





# Controllable synthesis of high-entropy alloys

Jingjing Liang,<sup>†a</sup> Guanghui Cao,<sup>†b</sup> Mengqi Zeng <sup>\*b</sup> and Lei Fu <sup>\*ab</sup>

Cite this: *Chem. Soc. Rev.*, 2024, 53, 6021

Received 11th January 2024

DOI: 10.1039/d4cs00034j

rsc.li/chem-soc-rev

High-entropy alloys (HEAs) involving more than four elements, as emerging alloys, have brought about a paradigm shift in material design. The unprecedented compositional diversities and structural complexities of HEAs endow multidimensional exploration space and great potential for practical benefits, as well as a formidable challenge for synthesis. To further optimize performance and promote advanced applications, it is essential to synthesize HEAs with desired characteristics to satisfy the requirements in the application scenarios. The properties of HEAs are highly related to their chemical compositions, microstructure, and morphology. In this review, a comprehensive overview of the controllable synthesis of HEAs is provided, ranging from composition design to morphology control, structure construction, and surface/interface engineering. The fundamental parameters and advanced characterization related to HEAs are introduced. We also propose several critical directions for future development. This review can provide insight and an in-depth understanding of HEAs, accelerating the synthesis of the desired HEAs.

## Key learning points

(1) Guidelines for understanding the controllable synthesis of HEAs toward property modification. (2) Fundamental understanding of HEAs and the influence parameters. (3) The advanced characterization of HEAs. (4) The main approaches to designing HEAs from the perspectives of composition, morphology, structure, surface, and interface. (5) Current and future development directions in this emerging field.

## 1. Introduction

The basic alloying strategy of incorporating a small number of minor components into a principal element for a long time has been proposed. The concept of high-entropy alloys (HEAs) was put forward simultaneously by Ye *et al.* and Cantor *et al.* in 2004,<sup>1,2</sup> where materials containing five or more elements (each with an atomic percentage from 5% to 35%) were generally assumed to form solid-solution alloys through sufficiently high configurational entropy. The novel design philosophy of alloying highlights the unexplored interior realm of multidimensional phase diagrams, greatly enriching the material library. Later, with the increasing exploration of HEAs, the definition of HEAs becomes wider.<sup>3–5</sup> In recent years, some HEAs have been demonstrated to exhibit many excellent properties, such as irradiation resistance,<sup>6</sup> high strength,<sup>7</sup> enhanced stability,<sup>8</sup> high catalytic activity,<sup>9,10</sup> efficient photothermal conversion,<sup>11</sup>

*etc.*, making them powerful candidates in structural applications,<sup>12</sup> energy,<sup>13–15</sup> therapeutics<sup>16</sup> and other fields.<sup>17</sup>

Compared with less-element alloys, there is a vast composition space due to the multi-elemental combinations in HEAs, which provides an excellent platform for material design and development. Random multielement mixing in HEAs creates complex atomic and electronic configurations and atomic-level heterogeneity. Consequently, the diversity of chemical species at the atomic level results in the loss of periodicity, as well as the compressive and tensile strain field. The electronic, vibrational and magnetic excitations would also be affected.<sup>18</sup> Additionally, multi-dimensional heterogeneity exists in HEAs, such as the chemical short-range order, tiny and closely spaced clusters, complexes, *etc.*, which would increase the resistance to dislocation motion and afford high strength.<sup>19</sup> Meanwhile, the complex atomic configuration endows HEAs with diverse binding sites and a near-continuous distribution of binding energies, laying the foundation for fine-adjusting binding energies to regulate reaction properties.<sup>9,20</sup>

The properties of HEAs are highly associated with the chemical composition, structure, morphology, surface, and interface. The selection and proportion of elements can affect the adsorption energy distribution pattern, further adjusting

<sup>a</sup> The Institute for Advanced Studies, Wuhan University, Wuhan 430072, China

<sup>b</sup> College of Chemistry and Molecular Sciences, Wuhan University, Wuhan 430072, China. E-mail: leifu@whu.edu.cn, zengmq\_lan@whu.edu.cn

<sup>†</sup> These authors contributed equally to this work.

the catalytic activity.<sup>21</sup> Additionally, the level of chemical disorder in HEAs is related to the specific alloying elements, which affects the defect physics and radiation performance.<sup>18</sup> These indicate that the composition design of HEAs is vital to achieving performance modification. Moreover, another feature originating from multielement alloying within vast composition space is the diverse structure in HEAs.<sup>22</sup> This is closely related to their properties and application. For instance, owing to the site-isolation effect, the PtCoNiInGaSn HEA with an intermetallic phase can offer ordered reaction environments to efficiently catalyze oxidative dehydrogenation of propane using CO<sub>2</sub>.<sup>23</sup> Liu *et al.* constructed multiple coherent interfaces in the Fe<sub>26</sub>Co<sub>25</sub>Ni<sub>20</sub>Cu<sub>15</sub>Al<sub>13.1</sub>Ga<sub>0.9</sub> HEA to attain the trade-off among strength, plasticity, and coercivity.<sup>24</sup>

Likewise, the morphology and surface of materials also play an important role in their performance and application scenario.<sup>25</sup> HEAs in the bulk form usually show great promise for structural applications.<sup>26</sup> For nanoscaled HEAs, high specific surface areas, abundant active sites, and facile electron

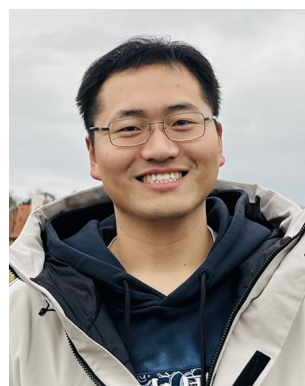
transport behavior make them promising for multiple surface reactions.<sup>27</sup> Therein, the morphology and surface of HEAs can be further designed to increase the atomic utilization or generate new interface interactions.<sup>28,29</sup> As a consequence, controllable synthesis of HEAs is the prerequisite for understanding the synthesis-to-structure-to-property correlations of materials and further realizing the property regulation as desired.

In response to the significant progress made recently in this field, here, we mainly summarize the controllable synthesis of HEAs (Fig. 1). First, the fundamental parameters and advanced characterization methods related to HEAs will be introduced, laying a solid foundation for the understanding of HEAs. Then, we will discuss the significance and strategies of the synthesis of HEAs with desired characteristics toward different applications from the perspective of composition design, morphology control, structure construction, and surface/interface engineering. Finally, current challenges and prospects will be proposed to further promote the exploration and developments in this rapidly emerging field.



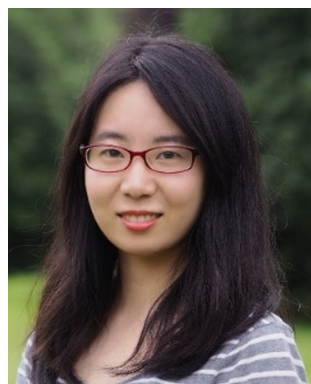
**Jingjing Liang**

*Jingjing Liang received her B.S. degree from the Shaanxi Normal University in 2019. She is currently a PhD candidate under the supervision of Prof. Lei Fu at the Institute for Advanced Studies at Wuhan University. Her current research is focused on the controllable synthesis of high-entropy materials and the exploration of related applications.*



**Guanghui Cao**

*Guanghui Cao received his B.S. degree from the Northeast Forestry University in 2019. He is currently a PhD candidate under the supervision of Prof. Lei Fu in the College of Chemistry and Molecular Sciences at Wuhan University. His current research is focused on the preparation of high-entropy alloys based on liquid metal and related application exploration.*



**Mengqi Zeng**

*Mengqi Zeng received her B.S. degree from the Wuhan University in 2013. She then received her PhD degree from the College of Chemistry and Molecular Sciences at Wuhan University. Now she works as a full professor at Wuhan University. Her current research is focused on the controllable synthesis and self-assembly of 2D materials on liquid metals.*



**Lei Fu**

*Lei Fu received his B.S. degree in chemistry from the Wuhan University in 2001. He obtained his PhD degree from the Institute of Chemistry, Chinese Academy of Sciences in 2006. After obtaining his PhD degree, he worked as a Director's Postdoctoral Fellow at the Los Alamos National Laboratory, Los Alamos, NM (2006–2007). Thereafter, he became an associate professor at Peking University. In 2012, he joined Wuhan University as a full professor. He developed the liquid metal growth system to manufacture advanced materials with atomic precision.*

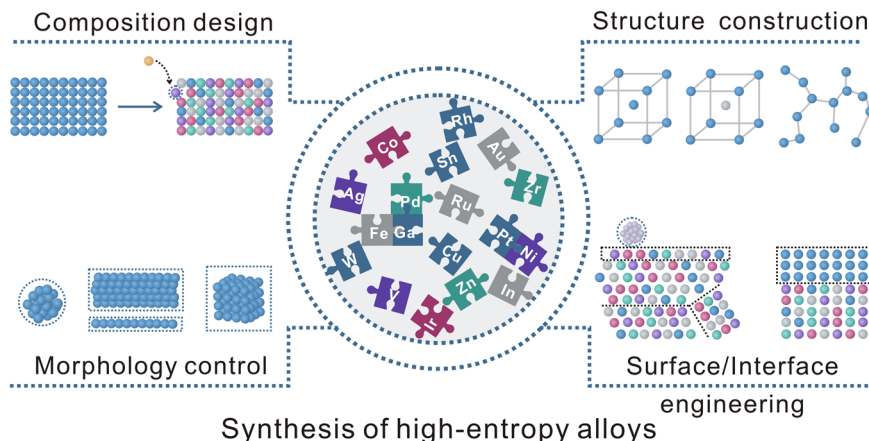


Fig. 1 Schematic illustration of the controllable synthesis of HEAs.

## 2. Fundamental parameters related to high-entropy alloy formation

The classical Hume-Rothery rules point out the principle of the formation of solid solution alloys, where similar atomic sizes, crystal structure, valency, and electronegativity of elements are in favor of the stabilization of solid solution alloys.<sup>30</sup> Based on the rules and thermodynamic consideration, researchers have mainly developed five influence factors to discuss the formation of HEAs, including mixing entropy, mixing enthalpy, atomic size difference, valence electron concentration, and electronegativity difference.<sup>22,31</sup> These parameters are relevant to the chemical composition of HEAs, which could be considered as the intrinsic regulation factors of HEA formation.

The mixing entropy ( $\Delta S_{\text{mix}}$ ) of alloys can be approximated as the configurational entropy ( $\Delta S_{\text{conf}}$ ), which can be formulated as follows:

$$\Delta S_{\text{mix}} = \Delta S_{\text{conf}} = -R \sum_{i=1}^n c_i \ln c_i$$

where  $R$  represents the mole gas constant, and  $c_i$  is the atom percentage of the  $i^{\text{th}}$  component, and  $n$  is the number of components in the alloys. When the content of multiple elements is in an equal molar ratio, it would generate a maximization of mixing entropy in alloys, where  $\Delta S_{\text{mix}}$  can be simplified as follows:

$$\Delta S_{\text{mix}} = R \ln(n)$$

Therefore, the mixing entropy increases with the number of elements. High mixing entropy would be conducive to the random occupancy of different elements at the site of the lattice. Under such circumstances, the generation of the ordered phase and phase separation could be restrained, promoting the formation of a solid solution phase.

George *et al.* discovered that mixing enthalpy plays a more important role than mixing entropy in phase stability for different quinary HEAs with equiatomic compositions.<sup>32</sup>

Actually, from the viewpoint of thermodynamics, it is the Gibbs free energy ( $\Delta G_{\text{mix}}$ ) that decides the phase formation.<sup>33</sup>

$$\Delta G_{\text{mix}} = \Delta H_{\text{mix}} - T\Delta S_{\text{mix}}$$

where  $T$  is the temperature and  $\Delta H_{\text{mix}}$  represents the mixing enthalpy. Therefore, it is essential to take mixing enthalpy into consideration.

The mixing enthalpy of HEAs describes the chemical compatibility, which can be expressed below.

$$\Delta H_{\text{mix}} = \sum_{i=1, i \neq j}^n 4\Delta H_{ij}^{\text{mix}} c_i c_j$$

where  $c_i$  or  $c_j$  is the atomic percentage of the  $i^{\text{th}}$  or  $j^{\text{th}}$ .  $\Delta H_{ij}^{\text{mix}}$  represents the mixing enthalpy of the atom pair between the  $i^{\text{th}}$  and  $j^{\text{th}}$  components. The positive value of mixing enthalpy reflects a repulsive interaction between components, increasing the tendency of phase separation or elemental segregation. When the mixing enthalpy is more negative, there is a strong attraction between elements, making it easier to generate intermetallic compounds. Moreover, Inoue reported that the very negative mixing enthalpy would promote the formation of the amorphous structure.<sup>34</sup> For nanoscale alloying, the size effect can be regarded as an additional negative mixing enthalpy which will help with the alloy mixing by lowering the Gibbs free energy, whose effect is mostly evident at a very small size, *e.g.* 3 nm.<sup>35</sup>

In addition to thermodynamic parameters, atomic size difference ( $\delta$ ), as a topological parameter, is also closely related to the stability of HEAs, whose calculated formula is shown as follows:

$$\delta = \sqrt{\sum_{i=1}^n c_i \left(1 - \frac{r_i}{\bar{r}}\right)^2}$$

$$\bar{r} = \sum_{i=1}^n c_i r_i$$

where  $\bar{r}$  is the average radius of all elements,  $r_i$  and  $c_i$  are the atomic radii and atomic percentage of the  $i^{\text{th}}$  element, respectively. If the atomic size difference is very large, the lattice would

undergo extremely severe deformation, destabilizing the solid solution structure and inducing phase transformation.<sup>36</sup>

The valence electron refers to the electrons that can interact with other atoms to form chemical bonding. Therefore, the valence electron concentration (VEC) of HEAs can affect the phase structure by regulating the characteristics of bonding and stacking, which can be calculated as follows:

$$\text{VEC} = \sum_{i=1}^n c_i (\text{VEC})_i$$

where  $(\text{VEC})_i$  represents the VEC of the  $i^{\text{th}}$  component,  $c_i$  is the percentage of atoms of the  $i^{\text{th}}$  component. It was reported that the VEC is closely associated with the relative stability of face-centered cubic close packing (FCC) and body-centered cubic packing (BCC) structures for some HEAs.<sup>37,38</sup>

Electronegativity represents the preference of atoms for electrons. The difference in the Pauling electronegativity ( $\Delta\chi_{\text{Pauling}}$ ) of HEAs is defined as follows:

$$\Delta\chi_{\text{Pauling}} = \sqrt{\sum_{i=1}^n c_i (\chi_i - \chi_{\text{avg}})^2}$$

$$\chi_{\text{avg}} = \sum_{i=1}^n c_i \chi_i$$

where  $c_i$  is the atomic percentage and  $\chi_i$  describes the Pauling electronegativity of the  $i^{\text{th}}$  component. Li *et al.* discovered that the stability of topologically close-packed phases could be evaluated by the parameter of  $\Delta\chi_{\text{Pauling}}$ .<sup>39</sup>

In short, mixing entropy has always been an important influencing factor for the formation of single-phase solid solutions. Mixing enthalpy depicts the atomic interaction between elements and could affect the microstructure of HEAs. The atomic size difference, valence electron concentration, and electronegativity difference parameters are related to the intrinsic attributes of atoms, which play a vital role in the phase stability, structural stacking character, and phase transformation of HEAs. These five parameters are closely related to the phase structure and element distribution of HEAs, which could further affect the performance. For example, raising the difference of the atomic size and electronegativity (*i.e.*, replacing Mn with Pd in the CrFeCoNiMn HEA) would enhance the effect of local aggregations, which led to considerable resistance to dislocation glide and thereby a higher yield strength.<sup>40</sup> Moreover, Liu *et al.* discovered that the introduction of the Ni element to form the strong enthalpic interaction between (Ni, Co) and (Al, Ti) pairs in the FeCrCoAlTi<sub>0.5</sub> HEA could cause the phase partitions into the A2 precipitate and the B2 matrix, which realized the combination of strength and plasticity.<sup>41</sup>

### 3. Advanced characterization methods of high-entropy alloys

Owing to the multi-component, HEAs possess complexity at the levels of atoms and electrons such as the lattice structure and

electronic structure, creating grand challenges in the characterization of HEAs. Taking the quinary HEAs as an example, the nearest neighboring atomic arrangement way of one atom in the FCC(111) face is more than  $10^5$ .<sup>42</sup> The complex atomic configurations make electronic structures of HEAs variable, further affecting their catalytic properties.

Some conventional techniques are applied for HEA characterization. Scanning electron microscopy (SEM), transmission electron microscopy (TEM), and X-ray diffraction (XRD) can be used for probing the morphology, size, composition, elemental distribution, and basic phase structure, giving the cognition of HEAs to some extent. Although these methods can supply much information about HEAs under most circumstances, there are still high requirements and necessity for the improvement of characterization techniques, aiming at gaining more detailed information, such as the chemical environment and bonding structure of specific atoms, and promoting the in-depth understanding of HEAs to decouple the multi-elemental mixing. The advanced characterization method would also bring a clearer interpretation of the mechanism and pathway of the reactions that HEAs participated in.

Advanced characterization techniques have been developed with high resolution and accuracy, which are suitable for exploring complicated systems. Characterization techniques based on synchrotron radiation (SR) possess the ultra-high resolution and signal-to-noise ratio.<sup>43</sup> The electronic structure of HEAs can be characterized *via* SR-based hard X-ray photoelectron spectroscopy (HAXPES), which is associated with the adsorption and binding energy of intermediates. Kitagawa *et al.* used HAXPES to demonstrate the valence band spectrum and d-band center of HEAs,<sup>42,44</sup> providing an opportunity to understand the origin of the enhanced hydrogen evolution reaction (HER) performance. SR-based X-ray absorption near-edge structure (XANES) is also a powerful technique for probing the electronic structure of HEAs. Zhang *et al.* reported that 3d metal elements (*i.e.* Co and Ni) exhibited different types of oxidation in different HEA systems *via* measuring the K-edge.<sup>45</sup> Besides, the SR-based extended X-ray absorption fine structure (EXAFS) can obtain the coordination number and bonding structure.<sup>45,46</sup> Synchrotron XRD can be used for identifying the phase structure and possible impurities in HEAs with great accuracy.<sup>47</sup>

In addition to the spectrum characterization based on the SR technique, the direct visual characterization is also of great importance. Taking the characterization of the atomic configuration and lattice structure as an example, their visualization can be realized *via* electron microscopy-based techniques. Short-range order (SRO) refers to the configuration where the atoms display a regular and ordered arrangement at a spatial scale that is usually less than 1 nm.<sup>48</sup> Considering the SRO reflects the specific configuration in the first and next couple of the nearest neighbors of atoms in HEAs or medium entropy alloys (MEAs),<sup>49</sup> the capture and characterization have been a challenging pursuit for years. Recently, the SRO was experimentally identified in a VCoNi MEA by using advanced and fine TEM characterization.<sup>50</sup> Both the selected area electron



diffraction pattern (EDP) and the corresponding nano-beam EDP with a high signal-to-noise ratio indicated that the extra disks between two transmission spots were highly diffused, which was explicit evidence for the existence of the SRO. The energy-filtered dark-field TEM image also directly observed the area where atoms exhibited the SRO structure. Furthermore, atomically energy-dispersive X-ray spectroscopy (EDS) mapping can identify the detailed arrangement of the SRO. For a further in-depth understanding of the SRO, an atomic electron tomography reconstruction method has been developed to reveal the 3D atomic position of amorphous HEA nanoparticles (HEA-NPs), indicating that the SRO could connect with each other to form medium-range order.<sup>51</sup> Moreover, four-dimensional scanning transmission electron microscopy (4D-STEM) enables the characterization of strain and local lattice distortion of HEA-NPs.<sup>47</sup> The advanced characterization techniques provide a single-atom-level insight into HEAs, promoting the understanding and development of the field.

## 4. Controllable synthesis of high-entropy alloys

Achieving superior performance in different applications has always been the major impetus for synthesizing and designing HEAs. With the growing exploration of HEAs, the number of aspects for the synthesis of HEAs with desired characteristics is likewise increasing to make the products meet the requirements of different application scenarios, which include the regulation of the composition, morphology, structure, surface, and interface.

### 4.1. Composition design

Chemical compositions could be considered as the roots of structures and the properties of alloys. With regard to the composition design of HEAs, the integration of multiple elements in an alloy (*i.e.* high-entropy state) is required first and foremost, which would supply the foundation for their particular performance. The concentration, category, and mixing state of elements are of great importance for the alloys. That is to say, the overall properties could also be modulated by the specific state of elements.

**4.1.1. High-entropy mixing.** Benefiting from the composition flexibility, high-entropy mixing greatly broadens the tuning range of the geometric and electronic properties of active sites, endowing HEAs with an almost continuous distribution of binding energies.<sup>20</sup> Thereby, the elemental type and concentration can be tailored to accommodate the optimum binding energy for catalytic reactions. Meanwhile, complex surface active sites of HEAs may lead to spatially varying adsorption of intermediates, providing promising access to circumvent the Sabatier principle.<sup>52</sup> Additionally, the highly adjustable composition allows for the fine-tuning of the d-band distribution filling around the Fermi level to enhance the interband transitions for improving light absorption properties and photothermal conversion performance.<sup>11</sup> The lattice distortion stemming

from the atomic size difference could stabilize a thermodynamic nonequilibrium state, decreasing the energy barrier of active species (*e.g.*, electrons and ions).<sup>14,53</sup> Meanwhile, the distortion-derived highly fluctuating elastic stress/strain field could influence the movements of crystalline defects for regulating the dislocation behavior.<sup>54</sup> The high entropy and sluggish diffusion tendencies of HEAs are recognized as the main impetus for enhancing thermodynamic and kinetic stabilities.<sup>20</sup> Moreover, owing to the disordered distribution of diversified constituent elements, high-entropy mixing could bring multiple levels of heterogeneities in HEAs.<sup>19</sup> When the load is applied and deformation occurs, the multiple heterogeneities in HEAs conduce to lattice friction and strain hardening, influencing the dislocation motion and promoting the strength–ductility synergy in mechanical properties. Therefore, the realization of high-entropy mixing possesses grand scientific and technological potential.

However, the huge difference in physicochemical properties hinders the uniform mixing of different elements. The early reported synthetic methods generated phase-separated structures in nanoalloys when diverse elements were mixed.<sup>55,56</sup> It is of great importance to overcome the immiscibility and obtain a high-entropy state in the composition design of HEAs. Based on the Gibbs free energy formula ( $\Delta G_{\text{mix}} = \Delta H_{\text{mix}} - T\Delta S_{\text{mix}}$ ), the uniform mixing and formation of the high-entropy state could be propelled through the adjustment of the three contained parameters (*i.e.*  $\Delta H_{\text{mix}}$ ,  $T$  and  $\Delta S_{\text{mix}}$ ).

Hu *et al.* proposed a carbothermal shock (CTS) strategy to synthesize HEA-NPs containing eight dissimilar elements, which makes the reaction to occur at ultrahigh temperatures (about 2000 K) within about 55 ms (Fig. 2a).<sup>57</sup> The improved temperature contributed to overcoming immiscibility gaps of components, as well as a decreased  $\Delta G_{\text{mix}}$ . Meanwhile, the ultrafast cooling rate is also essential to preserve the uniform high-entropy state and single-phase solid-solution structure. EDS mappings presented the uniform distribution of the eight elements, which demonstrated the formation of high-entropy mixing (Fig. 2b). Compared with the phase-separated alloy, the obtained PtPdRhRuCe HEA-NPs exhibited higher nitrogen oxide selectivity for ammonia oxidation, which likely originated from the highly homogeneous feature of the solid-solution structure (Fig. 2c). Additionally, the laser melting and arc melting strategy for the preparation of bulk HEAs also rely on the high temperature during the reaction to realize the high-entropy state. Similar to the CTS process, a series of non-equilibrium synthesis strategies featuring the “shock” could contribute to the simultaneous reduction, nucleation, and growth, leading to the formation of a high-entropy state. These developed strategies are simply summarized as follows: vapor phase oscillatory spark mixing,<sup>35</sup> fast-moving bed pyrolysis,<sup>58</sup> an ultrasonication-assisted method,<sup>59</sup> laser heating,<sup>60,61</sup> transient electrosynthesis,<sup>62</sup> a hydrogen spillover-driven method,<sup>63</sup> microwave heating,<sup>64</sup> chemical co-reduction,<sup>65</sup> and so on.<sup>66</sup> These synthesis strategies analogous to CTS are also applied to more kinds of high-entropy materials, such as multi-element oxide nanoparticles,<sup>67</sup> high-entropy carbide films,<sup>68</sup>

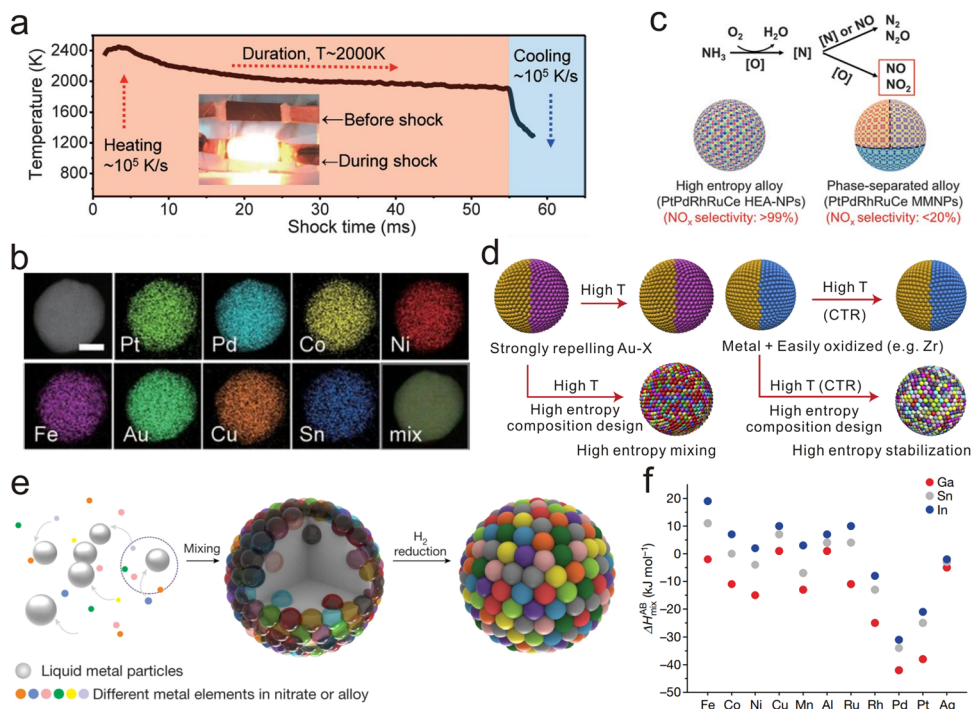


**Fig. 2** Realization of the high-entropy mixing state. (a) Temperature evolution with time in the carbothermal shock strategy. (b) STEM elemental maps of the individual octonary (PtPdCoNiFeCuAuSn) HEA-NP. (c) Schematic illustration of the ammonia oxidation process and the performance comparison between the HEA-NPs synthesized by the carbothermal shock strategy and the phase-separated alloy by wet impregnation. Reproduced from ref. 57 with permission from American Association for the Advancement of Science, Copyright 2018. (d) Schematic diagram of the strongly repelling pairs (left) and easily oxidized elements (right) stabilized by combining high temperature with the high-entropy strategy. Reproduced from ref. 47 with permission from Elsevier, Copyright 2021. (e) Schematic illustration of the liquid metal-assisted strategy for the HEA-NP synthesis. (f) Statistics diagram of the binary mixing enthalpy of liquid metals (Ga, Sn, and In) with other elements. Reproduced from ref. 70 with permission from Springer Nature, Copyright 2023.

and high-entropy metal sulfides,<sup>69</sup> which have enriched the composition of high-entropy materials.

Considering that the high mixing entropy conduces to the formation of a single-phase solid-solution structure, the parameter  $\Delta S_{\text{mix}}$  is also critical for high-entropy mixing. The mixing entropy could be raised by increasing the number of elements. Combined with the high reaction temperature, their contribution could be further amplified for multi-element mixing in consequences. The HEA-NPs up to 15 distinct elements are successfully synthesized by Hu *et al.* via the integration of high temperature and high entropy.<sup>47</sup> The elemental range of high-entropy mixing has been extended to the strongly repelling pairs (Au-W and Au-Mo) and easily oxidized elements (Zr) (Fig. 2d).

In addition to increasing the contribution of  $T\Delta S_{\text{mix}}$  for counterbalancing the enthalpy penalty and promoting high-entropy mixing, decreasing mixing enthalpy is another entry point for driving alloy formation. Fu *et al.* discovered that liquid metals can act as a reaction medium for the synthesis of HEAs by utilizing its feature of relatively negative mixing enthalpy with most metal elements to decrease the Gibbs free energy (Fig. 2e and f).<sup>70</sup> After introducing Ga, the ratio of compositions satisfying the criteria of the solid solution phase increased, demonstrating that mixing enthalpy is important for HEA formation. Besides liquid metal elements, the mixing enthalpy

between Pt and other metal elements is also mostly negative, which is also feasible for high-entropy mixing.<sup>71</sup>

Moreover, it was reported that the autocatalysis of some noble metal (e.g., Pd and Pt) atoms can realize high-entropy mixing.<sup>72,73</sup> The noble metal salts were preferentially reduced and nucleated in mixed precursors, which could then autocatalyze the other elements to be fully reduced and result in the formation of HEAs.

**4.1.2. Element modulation.** HEAs have been demonstrated to exhibit unexpected properties profiting from the integration of various elements in some studies. The modulation of specific elements would affect the atomic arrangement, elemental distribution, and phase structure, thus regulating performance.

Zheng *et al.* developed an atomic-level tailoring strategy to construct the paracrystalline HEA through the modulation of Pt.<sup>74</sup> Owing to the highly negative mixing enthalpy, the introduced Pt induced the rearrangement of its surrounding atoms, which tailored the crystalline HEA structure into the paracrystalline HEA with a structure of medium-range order and amorphization (Fig. 3a and b). Such structural characteristics endowed it with high yield strength and hardness (Fig. 3c).

A certain element also has a significant impact on entire elemental distributions in HEAs. Yu *et al.* replaced the Mn element with the Pd element in the CrMnFeCoNi Cantor alloy.<sup>40</sup> Compared with Mn and the other four elements, the

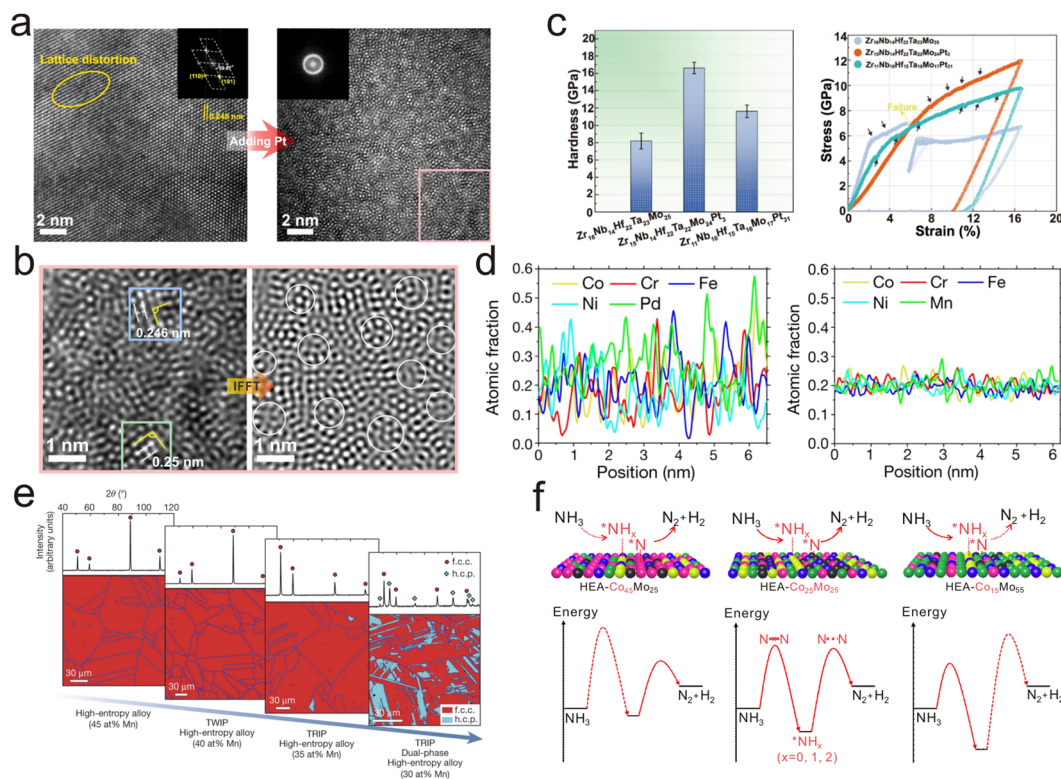


**Fig. 3** Modulation of elements in HEAs. (a) High-resolution TEM images with the corresponding FFT patterns (insets) of the HEA before (left) and after (right) adding Pt. (b) Magnified TEM images of the pink box in (a). The lattice spacings and angles of the medium-range order region are marked in the image. (c) The hardness results (left) and the stress–strain curves (right) of different HEAs. The Pt-3% HEA showed a paracrystalline structure. Reproduced from ref. 74 with permission from Springer Nature, Copyright 2023. (d) EDS line profiles of the atomic fraction of CrPdFeCoNi (left) and CrMnFeCoNi (right). Reproduced from ref. 40 with permission Springer Nature, Copyright 2019. (e) EBSD phase maps and corresponding XRD patterns of the HEA with different Mn concentrations. Reproduced from ref. 7 with permission from Springer Nature, Copyright 2016. (f) Schematic illustration of the  $NH_3$  decomposition mechanism in the HEAs with different Co/Mo ratios. Reproduced from ref. 75 with permission from Springer Nature, Copyright 2019.

Pd atom has the largest atomic radius and electronegativity, leading to fluctuations of atomic fractions and obvious element aggregation (Fig. 3d). Consequently, it generated the alternating compressive and tensile strain fields at the nanoscale, providing strong resistance to dislocation glide and thereby enhancing the yield strength. The atomic-level modulation strategy provides more access to purposefully regulate and optimize properties, meanwhile displaying the precision of the modulation.

Moreover, regulating the element concentration can realize the modulation of the phase structure. Tasan *et al.* designed a metastable HEA system with a dual-phase microstructure.<sup>7</sup> As the atomic fraction of Mn decreased from 45% to 30% in  $Fe_{80-x}Mn_xCo_{10}Cr_{10}$ , the hexagonal close-packed (HCP) phase appeared (Fig. 3e), which originated from the martensitic transformation of the FCC phase. Accordingly, the deformation mechanism changed, increasing the ductility and strength. In addition to mechanical performance, element modulation could also be applied to enhance the functional properties of HEAs. Wang *et al.* synthesized CoMoFeNiCu HEA-NPs with different Co/Mo ratios for the  $NH_3$  decomposition reaction.<sup>75</sup> The change of the element ratio modulated the adsorption and desorption properties of the catalytic process (Fig. 3f). HEA-NPs

with the  $Co_{25}Mo_{45}$  elemental ratio were demonstrated to be the most excellent catalyst.

Due to their vast compositional space and complex atomic structure, there are grand challenges to realizing the composition design of these intrinsically complex alloys toward property modification. High-throughput computational methods and combinatorial synthesis can explore the multielement space of HEAs more effectively than the traditional trial-and-error approaches.

Generally, four types of calculation methods have been demonstrated to accelerate the exploration rate of novel HEA compositions, which are empirical rules, calculation of phase diagrams, first-principles calculations, and machine learning.<sup>76</sup> As a viable method to investigate the thermodynamic and atomistic mechanisms of the HEAs, a chemical map of the equimolar single-phase HEAs was constructed through high-throughput density functional theory (DFT).<sup>77</sup> The computation following the empirical rules and the calculation of the phase diagram was capable of realizing the phase prediction of HEAs within millions of elemental composition space.<sup>78,79</sup> Additionally, the HEA composition with desired mechanical performance has been demonstrated to be screened out computationally.<sup>80</sup> It should be noted that these calculations



may not be easily transferred to the HEAs with the nanoscale size considering that they mainly build on the thermodynamic equilibrium consideration of materials at the microscale. Moreover, determining the active site for binding and building an accurate atomic model for exploring the structure–property performance are also great challenges for HEAs. Recently, machine learning tools have been increasingly utilized to accelerate performance prediction and guided optimization in the HEA field owing to strong learning ability and powerful processing of complex data. Rossmeisl *et al.* performed DFT and supervised learning to explore the optimized surface atomic configurations and predict the adsorption energy of the HEA catalyst toward the oxygen reduction reaction (ORR).<sup>81</sup> Utilizing the neural network and DFT method, the researcher tried to decouple the ligand and coordination effects of the HEA catalyst to explore the relationship between structural features and catalytic performance.<sup>82</sup>

Combinatorial synthesis and high-throughput characterization have been demonstrated to experimentally screen HEAs for discovering high-performance materials. Schuhmann *et al.* realized the combinatorial synthesis of different HEA-NPs by utilizing co-sputtering, which resulted in the discovery of a catalyst with high activity for the ORR.<sup>83</sup> Yao *et al.* achieved the high-throughput synthesis and characterization of HEA-NPs to rapidly screen these samples for highly active catalysts discovery based on ink-printed and scanning droplet cell techniques.<sup>84</sup> Moreover, the high-throughput experimentation could provide data feedback to refine the model of the computational prediction, which could also guide the experimentation and *vice versa*. Consequently, a closed-loop optimization protocol was established to advance the prediction power toward the discovery of the most active HEA composition.<sup>85</sup> Therefore, combinatorial high-throughput studies enable rapid prediction, synthesis, and characterization of promising HEA compositions in the vast compositional space.

## 4.2. Morphology control

The physicochemical properties and applications of materials are largely affected by their morphology, especially in the catalysis field.<sup>86</sup> Generally, downsizing HEAs to the nanoscale and constructing porous or hierarchical nanostructures can provide a large surface area and efficient electron/mass transport for elevating reaction kinetics and catalytic activity and improving atomic efficiency. In this part, the significance and approaches to regulating the morphology in zero-dimensional, one-dimensional, two-dimensional, and three-dimensional HEAs are discussed in detail.

**4.2.1. Zero-dimensional HEAs.** Nanoparticles (NPs), a kind of zero-dimensional material, are the major low-dimensional HEAs since the approach of carbothermal shock was reported in 2018.<sup>57</sup> Most of the strategies mentioned in Section 4.1.1 can achieve the preparation of HEA-NPs.<sup>57,58,65</sup> Thereinto, the supports are usually utilized to assist in controlling the size and alleviate the agglomeration of the HEA-NPs during the synthesis. The design of HEA-NPs would expose more specific

surface areas and reaction sites to enhance reaction kinetics and activity.

The wet-chemistry synthetic approach allows for the excellent control of the NP shape and size. The morphology of the material mainly depends on the relative magnitudes between the atom deposition rate ( $V_{\text{deposition}}$ ) and the surface diffusion rate ( $V_{\text{diffusion}}$ ), which can be regulated by the reagent concentration, capping agent, and injection rate.<sup>87,88</sup> Yang *et al.* reported the synthesis of distinctive HEA-NPs including the tetrahedral and dendritic shapes (Fig. 4a).<sup>89</sup> By increasing the injection rate, a higher  $V_{\text{deposition}}$  could be obtained. When the value of  $V_{\text{deposition}}$  was larger than that of  $V_{\text{diffusion}}$ , the nanocrystal would follow island growth mode and thus develop into the dendritic shape. The surface of dendritic HEA-NPs provided low-coordination defect sites, which would optimize the hydrogen adsorption and consequently enhance the HER activity (Fig. 4b and c). Kang *et al.* reported the design of the convex cube-shaped HEA-NPs by selective deposition of atoms with the assistance of the Ru element, which was demonstrated to be a high-activity catalyst toward water splitting and the ORR.<sup>90</sup> Besides, Hu *et al.* realized hollow nanostructures by utilizing the decomposition of citric acid to generate gas, which *in situ* puffed the NP into a hollow structure.<sup>28</sup> The interior void space of HEA-NPs would greatly increase atom economy, realizing a record current density per unit catalyst mass of 2000 mA g<sub>cat</sub><sup>−1</sup> for the Li–O<sub>2</sub> battery. In addition to individual NPs, the aggregation of HEA-NPs can be patterned in a controlled morphology by using the strong coordination interaction between metal cations and the bases of DNA origami template with a prescribed pattern.<sup>91</sup>

The optimization of the HEA-NP size can be achieved by enhancing the strength of reducing agents (*e.g.*, lithium naphthalenide) or enhancing the metal–substrate interaction (*e.g.*, defect engineering of the substrate).<sup>92,93</sup> When the size was further decreased to the sub-nanoscale region, the material could produce new properties through the hybridization of atomic orbitals owing to the strong quantum effects in the sub-nanoclusters.<sup>94</sup> Ga<sub>1</sub>In<sub>1</sub>Au<sub>3</sub>Bi<sub>2</sub>Sn<sub>6</sub> sub-nanoclusters with a size of 0.9–1.0 nm were synthesized by employing the phenylazomethine (DPA) dendrimer as a macromolecular ligand template (Fig. 4d). The intramolecular potential gradient induced by the Lewis basicity difference of the DPA could promote the layer-by-layer stepwise complexation of the metal salts on the DPA template, followed by the reduction of metal salts with NaBH<sub>4</sub>, enabling the delicate modulation of the HEA cluster with the size of sub-nanoscale.

With a further decreasing number of atoms, the exploration of single-atom catalysts (SACs) has momentum due to their unique geometric and electronic properties and great potential to explore catalytic structure–performance relationships at the atomic scale.<sup>95</sup> Tian *et al.* developed a movable type printing method to synthesize high entropy SACs with a composition of up to eleven metal elements (Fig. 4e).<sup>96</sup> After coating the dopamine hydrochloride on the printing template M-g-C<sub>3</sub>N<sub>4</sub> composed of a metal precursor and melamine, high entropy SACs were generated by a pyrolysis process. Thereinto, the



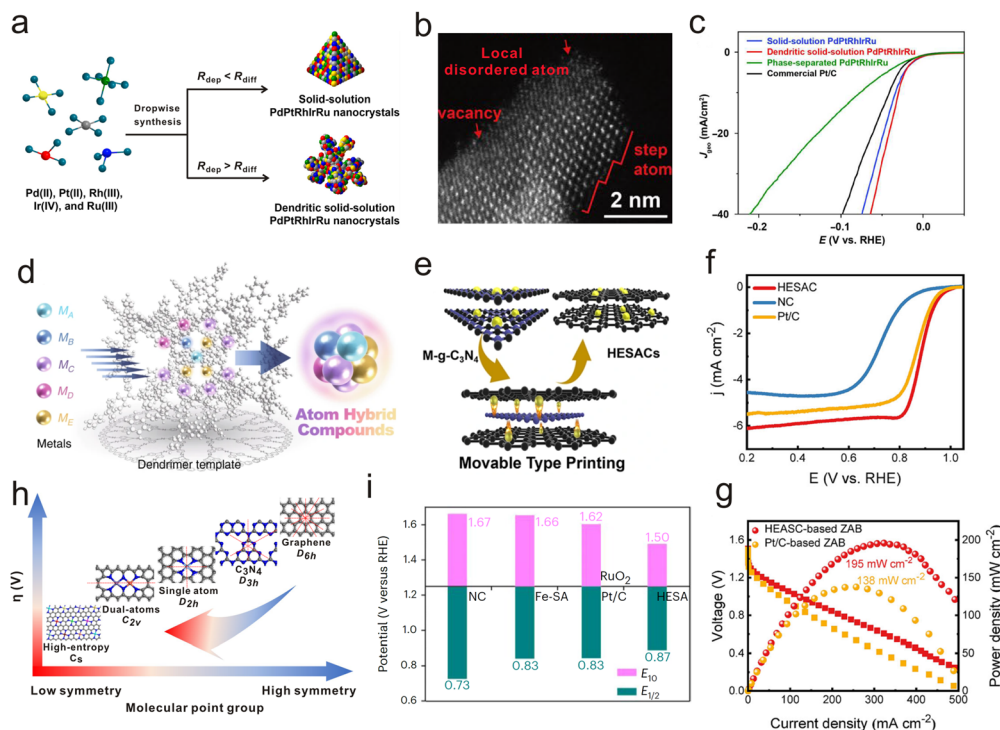


**Fig. 4** Synthesis of HEAs with the OD morphology. (a) Schematic illustration of the HEA nanocrystal formation with different shapes by manipulating the dropwise synthesis. (b) Atomic-resolution HAADF-STEM image of PdPtRhIrRu nanocrystals. (c) Electrocatalytic activity for the HER. Reproduced from ref. 89 with permission from American Association for the Advancement of Science, Copyright 2023. (d) Schematic illustration of the formation of sub-nanoclusters by using a dendrimer template. Reproduced from ref. 94 with permission from Springer Nature, Copyright 2018. (e) Schematic illustration of the movable type printing strategy to synthesize high-entropy SACs. (f) Electrocatalytic ORR activity of the quinary HESACs (FeCoNiCuMn). (g) Polarization and power curves of the Pt/C-based and HESAC-based zinc-air battery. Reproduced from ref. 96 with permission from Springer Nature, Copyright 2022. (h) The relationship between basal-plane symmetry and electrocatalytic activity. (i) The comparison of electrochemical ORR and OER performance. Reproduced from ref. 97 with permission from Springer Nature, Copyright 2023.

thermally excited and stripped metal atoms from M-g-C<sub>3</sub>N<sub>4</sub> were directly point-to-point transferred to the carbon support by the capture and stabilization of the defects and nitrogen species. The prepared quinary non-noble high-entropy SACs exhibited better activity than commercial Pt/C toward the ORR in the rotating disk electrode test and Zn-Air batteries (Fig. 4f and g). In addition to maximum atom utilization, the design of HEAs into the single atom state could decrease the local symmetry in graphitic carbon, inducing destabilization of the  $\pi$ -electron network to enhance the activity of carbon catalysts toward the oxygen evolution reaction (OER) and ORR (Fig. 4h and i).<sup>97</sup>

**4.2.2. One-dimensional HEAs.** One-dimensional (1D) materials with structural anisotropy present excellent properties, such as enhanced surface plasmon resonance and fast electron/mass transfer kinetics.<sup>98</sup> The high-entropy concept provides the 1D nanostructure with severe lattice distortion, which can vary the distribution of strain and electronic structure. Because most metals have cubic lattices with high structural symmetry, they tend to adopt the high symmetry morphology. To realize the anisotropic growth, the template or structure-directing agent was utilized to guide the deposition and diffusion of metal atoms.

Guo *et al.* utilized an Ag nanowire template to induce the anisotropic growth of HEAs (Fig. 5a).<sup>99</sup> The galvanic exchange

reaction enabled the nucleation and growth of different compositional metals on the Ag template accompanied by the co-reduction process. After a dealloying process, the inner Ag core was removed and HEA subnanometer ribbons were achieved. The abundant lattice distortion and defect of the subnanometer ribbons and the synergistic effect of multiple elements endowed them with a high mass activity 21 times higher than the Pt/C toward the ORR (Fig. 5b and c). Later, they developed a simple reduction-diffusion method, which increased the aspect ratio of the 1D nanostructure and generated HEA nanowires.<sup>100</sup> The *in situ*-produced CO molecule of Mo(CO)<sub>6</sub> could induce the initial nucleation of Pt to atomic-thick nanowires by selectively adsorbing on crystal faces. Then, the other metal atoms were reduced and diffused into the preformed nanowires. With the well-controlled morphology and tunable composition, the strain distribution and electronic structure of HEA nanowires could be regulated to realize outstanding catalytic performance. Moreover, both stearyl trimethyl ammonium bromide and hexadecyl trimethyl ammonium bromide (CTAB) have been demonstrated to act as structure-directing agents for producing HEA nanowires with numerous surface atomic steps and facet boundaries.<sup>101,102</sup> When carboxyl-functionalized surfactants are introduced as soft templates, it is possible to obtain HEA nanowire networks.<sup>103</sup>

**4.2.3. Two-dimensional HEAs.** Two-dimensional (2D) materials have attracted great attention owing to the quantum confinement effect.<sup>104</sup> In consideration of the non-directional metallic bonding and relatively high surface energy of the specific facet, it is extremely challenging to realize their 2D structure with single or few-atom layer thicknesses. Generally, the nanosheet and ultra-thin film could be regarded as the 2D structure of metals.<sup>105</sup> Kang *et al.* reported a pleated PdMoGaInNi nanosheet with an approximately 1.6 nm thickness as the excellent Pt-free HER electrocatalyst.<sup>106</sup> The reducing agent Mo(CO)<sub>6</sub> could *in situ* produce CO, which exhibited a strong adsorption tendency to the Pd (111) surface and resulted in the anisotropic growth of the PdMoGaInNi HEA. Moreover, in the presence of a CTAB surfactant, the formed Bi-complex nanosheet at the reaction beginning could act as a template to generate the PtRhBiSnSb nanosheet, which was demonstrated to be a state-of-the-art multifunctional material toward electrocatalytic electrooxidation reactions of methanol, ethanol, and glycerol.<sup>107</sup>

The liquid-phase synthesis usually generates 2D HEAs with a small in-plane size. Yang *et al.* reported the synthesis of free-standing HEA films with a lateral dimension at the centimeter

scale by combining multi-target magnetron sputtering with polymer surface buckling-enabled exfoliation.<sup>108</sup> When water molecules diffused into the PVA hydrogel substrate, it would spontaneously swell, leading to the exfoliation of the deposited metal film from the substrate within minutes and the formation of freestanding 2D HEAs with a thickness of about 36 nm (Fig. 5d). The obtained 2D FeCoNiCrNb film exhibited a lower elastic modulus than the corresponding thick film.

**4.2.4. Three-dimensional HEAs.** Introducing pores and even interconnected open channels into three-dimensional (3D) HEAs would greatly increase the specific surface area for exposing active sites and accelerating mass transfer. Dealloying is a facile strategy to realize the nanoporous structure by utilizing the Zn or Al metal as sacrificial elements.<sup>109,110</sup> Moreover, Liu *et al.* synthesized PdCuAuAgBiIn HEA aerogels *via* the freeze-thaw strategy,<sup>111</sup> which dramatically improved the porosity. Due to the strong interactions between the surface unsaturated sites in the porous structures and different metals of HEAs, the obtained PdCuAuAgBiIn aerogel exhibited impressive carbon dioxide reduction reaction performance (Fig. 5e and f), outperforming the corresponding HEA-NPs and Pd metallic aerogels. The faradaic efficiency (FE) of C1

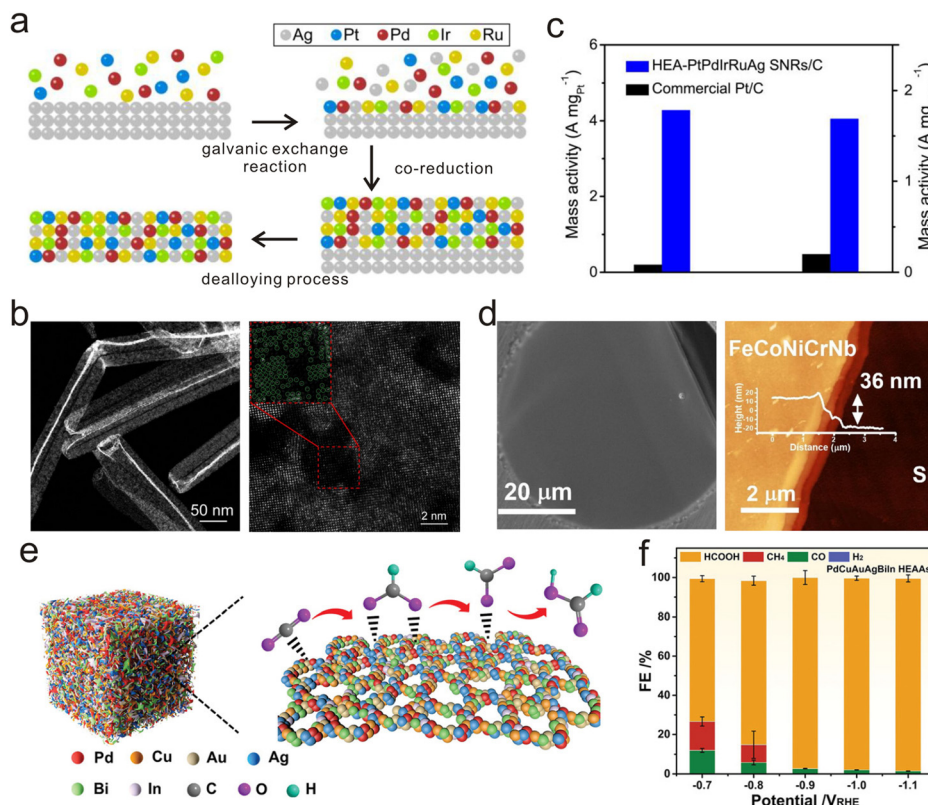


**Fig. 5** Synthesis of HEAs with 1D, 2D, and 3D morphologies. (a) Schematic illustration of the synthesis of HEA subnanometer ribbons. (b) Low-magnification (left) and high-resolution (right) HAADF-STEM images of the PtPdIrRuAg HEA subnanometer ribbon and the magnified atomic-resolution HAADF-STEM image (red dashed square). (c) Comparison of mass activity normalized with Pt and Pt group metals (PGM) at 0.9 V *versus* RHE. Reproduced from ref. 99 with permission from American Chemical Society, Copyright 2022. (d) SEM image (left) and AFM image (right) of the 2D FeCoNiCrNb HEA films. Reproduced from ref. 108 with permission from Elsevier, Copyright 2020. (e) Schematic illustration for enhanced HCOOH generation on PdCuAuAgBiIn HEA aerogels. (f) Reduction potential dependent faradaic efficiency (FE) tested on PdCuAuAgBiIn HEA aerogels. Reproduced from ref. 111 with permission from Wiley-VCH, Copyright 2022.

products is almost 100% from  $-0.7$  to  $-1.1$  V *versus* reversible hydrogen electrode ( $V_{\text{RHE}}$ ), and the maximum FE of formic acid can reach up to 98.1% at  $-1.1$   $V_{\text{RHE}}$ .

### 4.3. Structure construction

Although high configuration entropy endows HEAs with a tendency to form the solid solution phase, HEAs can also exist as intermetallics, the amorphous phase, and quasicrystal. It has been well-known that the structure determines the properties to a great extent. For example, the crystal structures are closely related to the electronic structure and electrical conductivity, which affect the activity and selectivity of catalytic reactions.<sup>112</sup> The construction of HEAs with desired structures is necessary for practical applications.

**4.3.1. Solid solution.** When the atoms of the alloy components exhibit a random distribution across the lattice, it is conventionally regarded as a solid solution. In HEAs, the most widely studied phase structure would be a solid solution structure, which has been realized *via* the majority of the approaches mentioned in Section 4.1.1, such as high-temperature shock, fast-moving bed pyrolysis, and so on.<sup>57,58,113</sup> It mainly consists of three simple phases, BCC, FCC, and HCP structures,<sup>22</sup> where the stacking structure forms in HEAs are highly related to the intrinsic elemental properties. HEAs with the BCC structure basically consist of refractory elements, which usually possess high strength. FCC-structured HEAs are predominantly composed of 3d transition metals and noble metals, which exhibit higher ductility than HEAs with the BCC phase. Meanwhile, most of the 3d transition metals and noble metals are catalytically active, allowing the HEAs with the FCC structure great potential for catalysis. For the HCP structure, it has been reported that rare earth elements tend to adopt HCP structural stacking.<sup>114</sup> Compared with cubic BCC and FCC phases, the HCP structure inherently has relatively less independent slip systems and suffers from intrinsic brittleness.<sup>115</sup>

**4.3.2. Intermetallic.** The intermetallic with ordered atomic structures and well-defined sublattices of the constituent elements features strong chemical bonding and site-isolation effect.<sup>116,117</sup> Such a structure enables the homogeneity of the active sites, which can help to study the underlying structure–activity relationship. Moreover, cubic B2 and  $L1_2$ -type structures have been designed in bulk HEAs to enhance strength and ductility.<sup>116,118,119</sup>

Thermal annealing is the most straightforward and effective protocol to produce the intermetallic by facilitating atom diffusion and ordering. Hu *et al.* reported a general strategy to generate high entropy intermetallic nanoparticles (HEI-NPs) *via* a disorder-to-order phase transition process (Fig. 6a).<sup>120</sup> After heating the disordered solid-solution HEA-NP intermediates, the sample underwent an atomic rearrangement toward an energetically more stable ordering configuration. Followed by rapid cooling, the high entropy intermetallic structure was finally locked in place. The HEI-NP existed as an  $L1_0$  structure with two sublattices, where Pt, Au, and Pd randomly occupied one sublattice and Fe, Co, Ni, Cu, and Sn casually distributed in the other sublattice (Fig. 6b). Moreover, Luo *et al.* found that

the FeCoNiCuPd HEA-NPs adopt two different phases by annealing treatment under an  $\text{NH}_3$  and  $\text{N}_2$  atmosphere.<sup>121</sup> The theoretical calculation indicated that  $\text{NH}_3$  prefers to absorb the HEI-NPs while  $\text{N}_2$  has a stronger affinity to FCC HEA-NPs. Therefore, annealing under an  $\text{NH}_3$  atmosphere would promote the atom reconstruction to a more favorable intermetallic structure. Owing to the stable chemically ordered structure and modulated electronic structure, the HEI-NPs exhibited better activity and durability toward the ORR than disorder HEA-NPs.

Although high-temperature annealing is beneficial to atom ordering, it also inevitably prompts metal sintering, resulting in particle growth and agglomeration. Liang *et al.* presented the synthesis of Pt-based HEI-NPs with an average size of  $< 5$  nm by a sulfur-anchoring approach (Fig. 6c).<sup>122</sup> The anchoring support was prepared by doping sulfur atoms in the porous carbon matrix. The strong metal–substrate interaction through Pt–S bonds could greatly inhibit the sintering of NPs up to 1273 K during the disorder–order transition process.

In addition to external energy regulation for circumventing the kinetic energy barrier involved in the atom ordering, the site occupation preference of an element also highly depends on the chemical composition. Furukawa *et al.* utilized intermetallic PtGe with strongly negative formation enthalpy as a structural framework to maintain the ordered structure upon multiple metal alloying (Fig. 6d).<sup>123</sup> The smooth substitution of Pt and Ge sites should be near elements in the periodic table for each, which would be helpful to the preservation of the parent PtGe-type structure. For the replacement of the Pt site, noble metals and Ni with high activity for C–H scission should be excluded, which enabled the Pt site to be “catalytically” isolated to suppress side reactions. The combination of high entropy and the site-isolation effects of the ordered structure allowed the (PtCoCu)(GeGaSn) HEI to exhibit high catalytic activity and thermal stability even at 600 °C during the propane dehydrogenation process (Fig. 6e and f). Meanwhile, the other catalysts exhibited slow deactivation because of coke accumulation. Such a strategy with partial substitution in the parent binary intermetallic has been demonstrated to be feasible in other HEI systems.<sup>23,124,125</sup> Moreover, the element selection containing the same binary intermetallic structure can realize the formation of the PtRhBiSnSb HEI.<sup>107</sup>

**4.3.3. Amorphous phase.** The amorphous alloy, also named metallic glass, usually possesses unique mechanics and catalytic properties due to the absence of long-range order in the atom arrangement.<sup>126,127</sup> According to the confusion principle, high mixing entropy also favors the formation of an amorphous phase.<sup>128</sup> It has been reported that a large atomic radius difference and very negative mixing enthalpy could enable high glass-forming ability,<sup>34</sup> which is beneficial to the preparation of metallic glass. However, it is difficult to avoid the nucleation and growth of crystals during the liquid–solid transition. The amorphous HEAs usually exist in the form of bulk metallic glasses, which were prepared by fast enough cooling the supercooled liquid to avoid crystallization. Recently, Dick *et al.* reported a nanodroplet-mediated



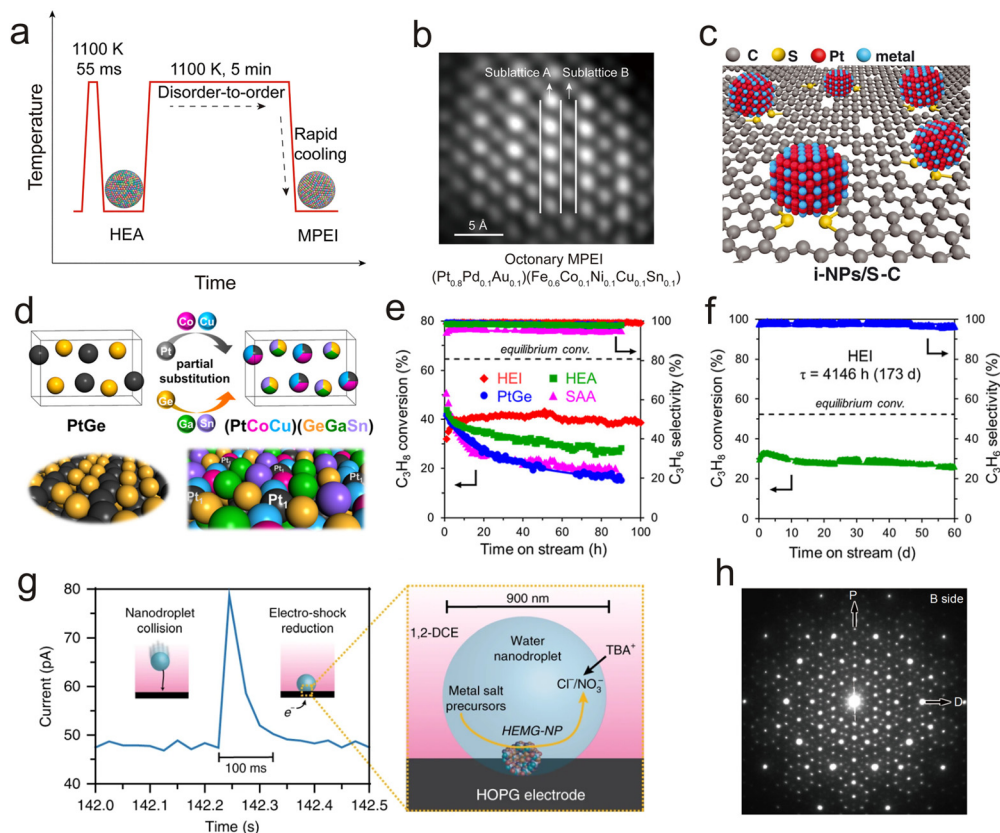


**Fig. 6** Construction of the intermetallic, amorphous, and quasicrystal structures in HEAs. (a) Temperature evolution with the heating time in the synthesis process of the HEI-NPs. (b) HAADF-STEM image of an octonary HEI-NP with the  $L1_0$  intermetallic structure. Reproduced from ref. 120 with permission from American Association for the Advancement of Science, Copyright 2022. (c) Illustration of the sulfur-anchoring strategy with high temperature. Reproduced from ref. 122 with permission from American Association for the Advancement of Science, Copyright 2021. (d) Illustration of the design concept for the HEI using the partial substitution strategy, forming the thermally stable isolated Pt active sites. (e) Catalytic performance of different catalysts in propane dehydrogenation without co-feeding  $H_2$  at 600 °C. (f) Stability of the HEI catalyst in propane dehydrogenation with co-feeding  $H_2$  at 600 °C. Reproduced from ref. 123 with permission from American Chemical Society, Copyright 2022. (g) Current variation along with the time during the synthesis process (left). The insets show the formation process of the amorphous HEA-NP. The schematic illustration of amorphous HEA-NP formation at the nanodroplet/electrode interface (right). Reproduced from ref. 62 with permission from Springer Nature, Copyright 2019. (h) SAED pattern of the quasicrystal structure along the tenfold direction. Reproduced from ref. 131 with permission from Science China Press and Springer-Verlag GmbH Germany, part of Springer Nature, Copyright 2020.

electrodeposition strategy to synthesize amorphous HEA-NPs with up to eight principle components (Fig. 6g).<sup>62</sup> A nanodroplet was created by confining various metal salt precursors to water nanodroplets emulsified by dichloroethane. After the nanodroplet collided with an electrode and was then reduced, NPs were electrodeposited into an amorphous microstructure within a 100 ms period. Moreover, slowing crystallization kinetics by ion implantation or stabilizing the amorphous phase by carbon species could also promote the realization of HEA-NP glasses in the reported studies.<sup>129,130</sup>

**4.3.4. Quasicrystal.** Different from amorphous solid and periodic crystals, quasicrystals possess long-range order without translational symmetry. Such a structurally complex phase is generally dominated by only one element. He *et al.* found the decagonal quasicrystal (DQC) in  $Al_{20}Si_{20}Mn_{20}Fe_{20}Ga_{20}$  melt-spun alloy ribbons.<sup>131</sup> By referring to similar structural blocks of DQCs, the Al-Si-Mn-Fe-Ga system was selected because there was a similarity between the reported Ga-Mn

and Al-Cr-Fe-Si decagonal quasicrystals about their 2 nm decagons. The diffraction spots in the selected area electron diffraction pattern (SAED) exhibited evident tenfold symmetry, indicating the existence of the DQC (Fig. 6h). The configuration entropy of both the HEA ( $Al_{20}Si_{20}Mn_{20}Fe_{20}Ga_{20}$ ) and the DQC ( $Al_{20.5}Si_{19.0}Mn_{20.9}Fe_{26.3}Ga_{13.3}$ ) was higher than 1.5R, which satisfied the definition of HEAs. Later, they further explored the phase transition in this quasicrystal HEA system.<sup>132</sup>

#### 4.4. Surface/interface engineering

Surface and interface play an important role in diverse applications, which are regarded as the main places where numerous physical and chemical transformation processes occur. Designing and optimizing surface/interface are proven feasible and effective strategies to enhance the performance of HEAs, such as catalysis and mechanics. In this part, we mainly concentrate on the surface of HEAs at the nanoscale and the interfaces of phases.



**4.4.1. Surface modification.** The surface of HEAs could be introduced to additional substances to realize modification, which is expected to reduce the catalyst cost by exposing the most active sites and improve their properties by interface interaction for various applications.

Yao *et al.* developed a two-step heating strategy to achieve the decoration of metallic elements on HEA-NPs.<sup>133</sup> Due to adopting a lower temperature and a shorter duration during the second step, the decorated Pd was mostly alloyed with the surface atoms of non-noble HEA-NPs (NHEA-NPs) by limiting atom diffusion, thus generating a surface-modified HEA catalyst (denoted as NHEA@NHEA-Pd) (Fig. 7a). Such a surface modification strategy simultaneously provided the catalyst with high stability and minimum usage of noble metals, where the NHEA core ensured that high entropy stability and active noble metal Pd only existed on the surface. As a result, the NHEA@NHEA-Pd catalyst achieved high mass activity and excellent stability in the ethanol oxidation reaction (Fig. 7b and c). Meanwhile, they also realized the Pt and Ir cluster decoration on the HEA-NP surface as the highly efficient electrocatalyst for overall water splitting.<sup>134</sup> Owing to the differences in reduction potentials, the Pt or Ir clusters were able to be anchored onto the surface of the FeCoNiCu or FeCoNiCrMn alloy using galvanic replacement, respectively.

Furthermore, Pt dendrites could be decorated on the surface of HEAs to construct a core-satellite heterostructure electrocatalyst (HEA@Pt).<sup>135</sup> The growth of Pt dendrites on the HEA was related to an autocatalytic behavior of Pt.<sup>136</sup> Owing to the difference in work functions, the atomically connected interface between Pt and HEA (Fig. 7d) would generate electron transfer of the heterointerface and further regulate the electron distribution, which provided abundant active sites and accelerated reaction kinetics. The d band center of the interfacial atoms changed because of the electron redistribution, affording appropriate adsorption energy of the intermediate to achieve superior ORR and OER performance (Fig. 7e).

In addition to metal elements, the surface of HEA-NPs could also be decorated by the non-metallic composition. An arc-discharged plasma method was developed to synthesize core@-shell structural HEA@graphite nanocapsules (Fig. 7f).<sup>29</sup> The surface of HEA-NPs was *in situ* modified by a few layers of graphite in the one-step encapsulation process through the decomposition of methane. The heterogeneous interface of the HEA core and the graphite shell could induce dielectric polarization. By regulating the composition of the HEA core, the polarization could be reinforced, realizing desirable electromagnetic wave absorption performance (Fig. 7g).

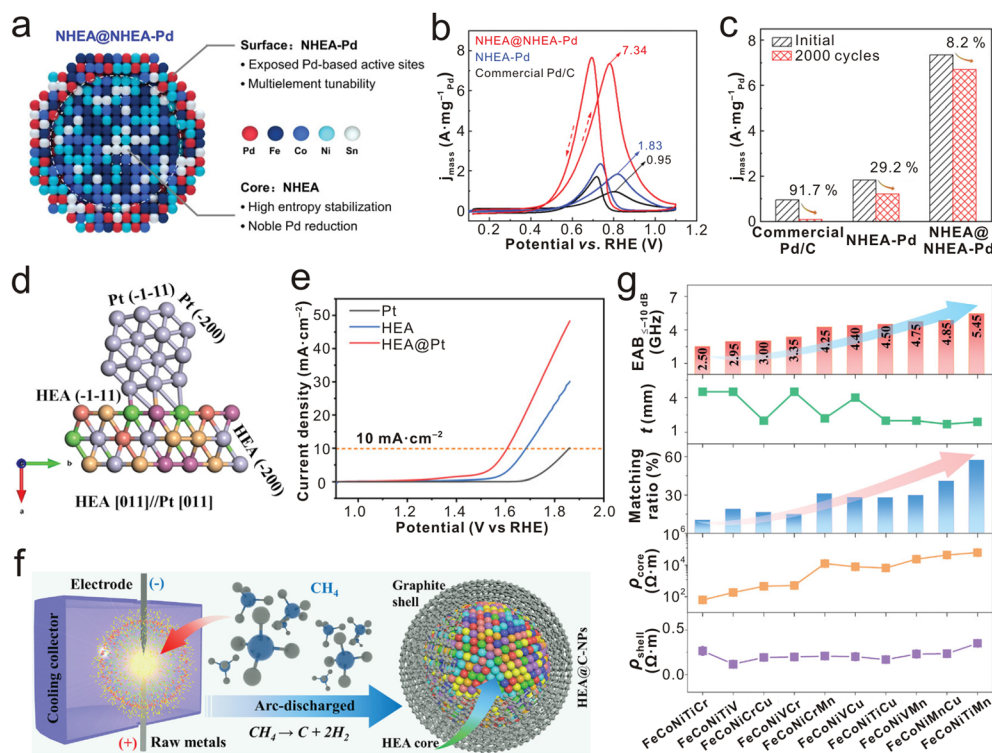


**Fig. 7** Surface modification of HEAs. (a) Scheme illustration of the NHEA@NHEA-Pd catalyst. (b) Mass activities of different catalysts for the electrocatalytic EOR. (c) Comparison of the stability of different catalysts for the electrocatalytic EOR after 2000 cycles. Reproduced from ref. 133 with permission from Wiley-VCH, Copyright 2022. (d) The crystal structure of Pt dendrites grown on HEAs, with an orientation relationship of HEA[011]//Pt[011]. (e) Electrocatalytic activity for the OER. Reproduced from ref. 135 with permission from Wiley-VCH, Copyright 2023. (f) Schematic illustration of the synthesis of HEA@graphite nanocapsules by using the arc-discharged method with the decomposition of methane. (g) Summary of the efficient absorption bandwidth below  $-10$  dB, with the corresponding thickness, the impedance matching ratio of HEA@graphite nanocapsules, and the resistivity of graphitic shells or HEA cores for different samples. Reproduced from ref. 29 with permission from Wiley-VCH, Copyright 2022.

**4.4.2. Surface reconstruction.** Many studies demonstrated that HEAs exhibited good stability under different electrochemical conditions and even high-temperature thermal catalysis, particularly compared with the less-element counterparts.<sup>71,123,125,135</sup> From the perspectives of thermodynamics and kinetics, it could be attributed to high entropy and sluggish diffusion tendencies.<sup>4,113</sup> The *in situ* TEM characterization revealed the excellent stability of the structure and the particle size distribution at temperatures up to 873 K.<sup>78</sup> Interestingly, surface reconstruction has also been experimentally observed in some HEAs. Such a unique behavior is also an emerging strategy to tune the elemental distribution and lead to unexpected properties.<sup>137</sup> The induction factors of surface reconstruction involve oxidation, heat treatment, and electrochemical redox.

*In situ* TEM revealed the surface oxidation process of PtFeCoNiCu HEA nanoparticles (Fig. 8a).<sup>138</sup> After annealing at 673 K for 40 min, the transition metals (Fe, Co, Ni, and Cu) exhibited preferential surface segregation to evolve into the oxide shell, while Pt remained in the core of the nanoparticle (Fig. 8b). By contrast, pure Co NPs suffered from catastrophic oxidation within about 1 min (Fig. 8c). The *in situ* experimental characterization during the oxidation process and dynamic simulations revealed the oxidation guided by the Kirkendall effect drove the elemental segregation.

Thermal treatment can promote atom rearrangement, providing accessible access to inducing surface reconstruction. Yang *et al.* synthesized the PtPdFeCoNiSnMn HEA possessing a PtPd-rich surface (Fig. 8d).<sup>139</sup> The HEA was obtained by using a solvothermal strategy, and the followed relatively low-temperature annealing could form the gathering of Pt and Pd on the surface. The segregation of Pt and Pd endowed a unique surface structure of the HEA with low-platinum-group-metals, leading to a performance with a high power density and superior stability in the direct ethanol fuel cell (Fig. 8e and f).

The surface reconstruction phenomenon of catalysts under electrochemical reaction conditions has been reported in many studies.<sup>140,141</sup> Recently, Ito *et al.* discovered that the redistribution of elements and the rearrangement of the surface structure occurred in novenary HEAs when the target reaction conditions were applied (Fig. 8g).<sup>142</sup> The rearranged surface of the HEAs was more conducive to the catalytic reaction, demonstrating high corrosion resistance as well as high catalytic activity in the practical application of water electrolysis.

**4.4.3. Interface design of phases.** In some cases, single-phase HEAs showed limitations for performance enhancements; for example, single-phase BCC HEAs possess high strength and low ductility while FCC HEAs are the opposite.<sup>22</sup> Surprisingly, the coexistence of various phases in HEAs brings a giant leap for some applications and properties owing to

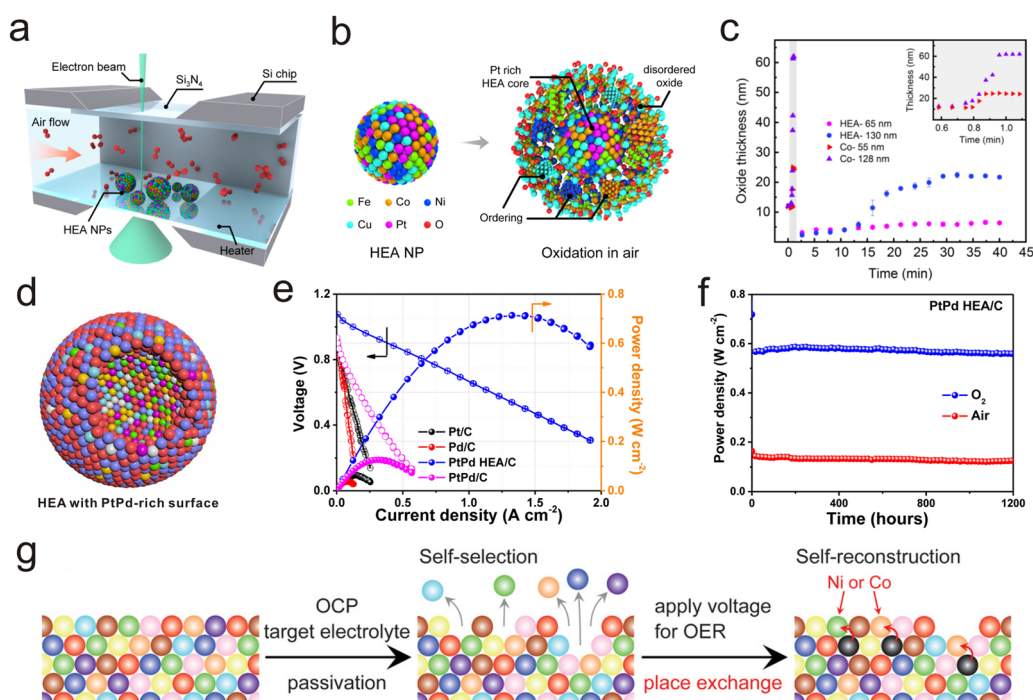


**Fig. 8** Surface reconstruction of HEAs. (a) Illustration of the TEM gas-cell for the *in situ* experiment. (b) Schematic illustration of the elemental segregation in PtFeCoNiCu HEA-NPs during the oxidation process. (c) The oxidation kinetics of HEA NPs and Co NPs with different sizes. Reproduced from ref. 138 with permission from American Chemical Society, Copyright 2020. (d) Schematic of the PtPdFeCoNiSnMn HEA with the PtPd-rich surface. (e) The steady-state polarization curves and power-density curves of the direct ethanol fuel cells utilizing different catalysts for membrane electrode assembly. (f) The discharge curves of the direct ethanol fuel cells at 0.6 V using the PtPdFeCoNiSnMn HEA as the catalyst. Reproduced from ref. 139 with permission from Elsevier, Copyright 2023. (g) Schematic illustration of the self-selection/reconstruction process on the HEA surface. Reproduced from ref. 142 with permission from Wiley-VCH, Copyright 2022.

multiphase interactions and interfacial effects. The phase interfaces create structural discontinuity, facilitate the chemical and electronic interactions between adjacent domains, and generate dislocation-precipitate phase interactions, endowing the materials with collective properties that are not observed in the single-phase structure. For example, the interface charge transfer can alter the plasmonic and catalytic properties.<sup>143,144</sup> In the case of the epitaxially grown multiphase structure, the generated strain can modulate the electronic structure.<sup>145</sup> There may be defects between the interface of the two domains for enhancing catalysis.<sup>146</sup> Moreover, the coherent or semicoherent interfaces conduce to improve the strength and maintain high ductility.<sup>147</sup>

Eutectic HEAs exhibit unique interfaces of phases due to their hierarchical microstructure.<sup>148</sup> The interface design and fabrication of eutectic HEAs have been invariably explored till now. Zhong *et al.* constructed the interface of the lamellar phase in eutectic HEAs by directional solidification.<sup>118</sup> The as-prepared eutectic HEA possessed a herringbone-like structure (Fig. 9a), which was composed of aligned and branched eutectic colonies. All of the eutectic colonies exhibited the hierarchical microstructure, comprising hard B2 and soft L1<sub>2</sub> lamellae. The alloy exhibited a high uniform elongation and extreme crack tolerance (Fig. 9b), which could be attributed to the effect of guiding and buffering on cracks devoted by the interface. Specifically, the soft L1<sub>2</sub> lamellae phase could hinder the crack from percolating forward and shield high local strains at crack

tips. Therefore, the microcracks that emerged in the hard B2 phase could be effectively arrested at the lamellar interface to the adjacent soft L1<sub>2</sub> buffer (Fig. 9c). Moreover, the interface between lamellae could also be fabricated *via* the strategy of laser powder bed fusion.<sup>12</sup> In this work, the HEAs realized a high yield strength as well as a large uniform elongation, whose thicknesses of lamellae could decrease to the nanoscale (Fig. 9d). With the applied strain increase, the edge dislocation density of the interface would increase while the nanolamellar did not exhibit a dramatic increase in the dislocation density (Fig. 9e and f), demonstrating that phase interfaces possessed the capability of dislocation storage. As a result, the dislocations could be effectively blocked and stored by the nanolamellae interfaces, which was beneficial to promoting the realization of strength-ductility synergy.

In addition to enhancing performance by lamellae interfaces mentioned above, it has been reported that precipitation in HEAs also contributes significantly to the properties *via* “precipitation-hardening”. Liu *et al.* constructed an interface of intermetallic nanoprecipitation and the FCC matrix in the HEA *via* arc melting and following thermomechanical treatments.<sup>149</sup> The high-density nanoprecipitation with the L1<sub>2</sub> structure was evenly located in the FCC matrix, whose size was about 30–50 nm (Fig. 10a). There was a small lattice mismatch of the dual-phase interface (Fig. 10b), which avoided heterogeneous coarsening and improved the stabilization of the nanoprecipitation. When the stress was applied and

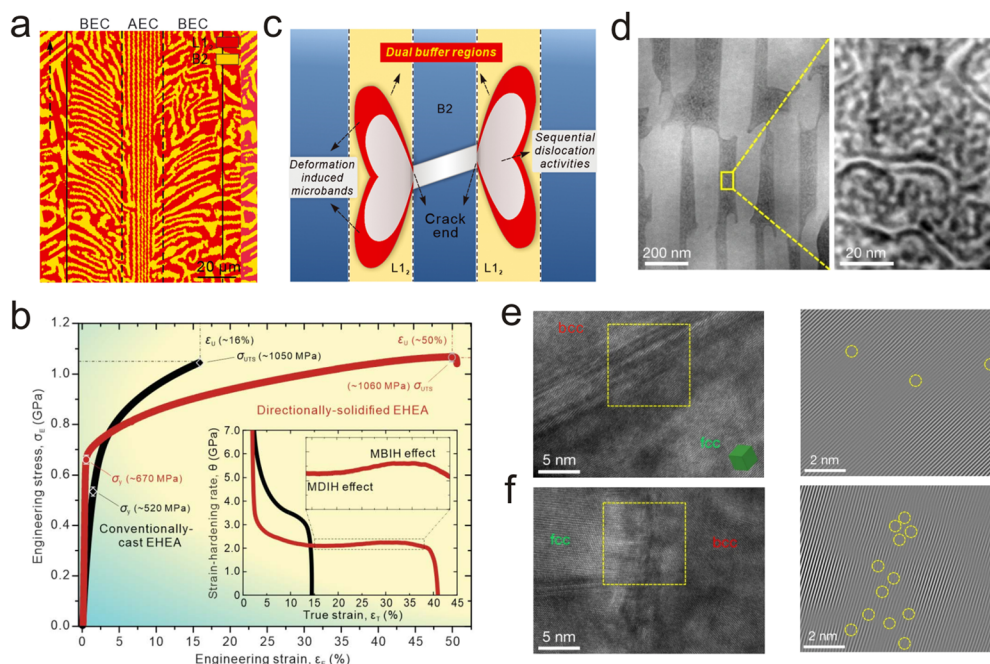


**Fig. 9** Construction of lamellar phase interfaces in HEAs. (a) Electron backscattering diffraction image of AEC and BEC with dual phases. (b) Engineering stress–strain curves of eutectic HEAs prepared *via* directional solidification and conventionally cast, respectively. Inset: The corresponding strain-hardening curves of the two alloys. (c) Schematic illustration of the buffering mechanism for crack. Reproduced from ref. 118 with permission from the American Association for the Advancement of Science, Copyright 2022. (d) HAADF-STEM image of the alternating FCC and BCC nanolamellae (left) and the magnified nanostructures within BCC lamellae (right). (e) and (f) HRTEM image (left) of the interface between FCC and BCC phases and the corresponding inverse FFT result (right) of the yellow box at tensile strains of about 0% (e) and 5% (f), respectively. Reproduced from ref. 12 with permission from Springer Nature, Copyright 2022.



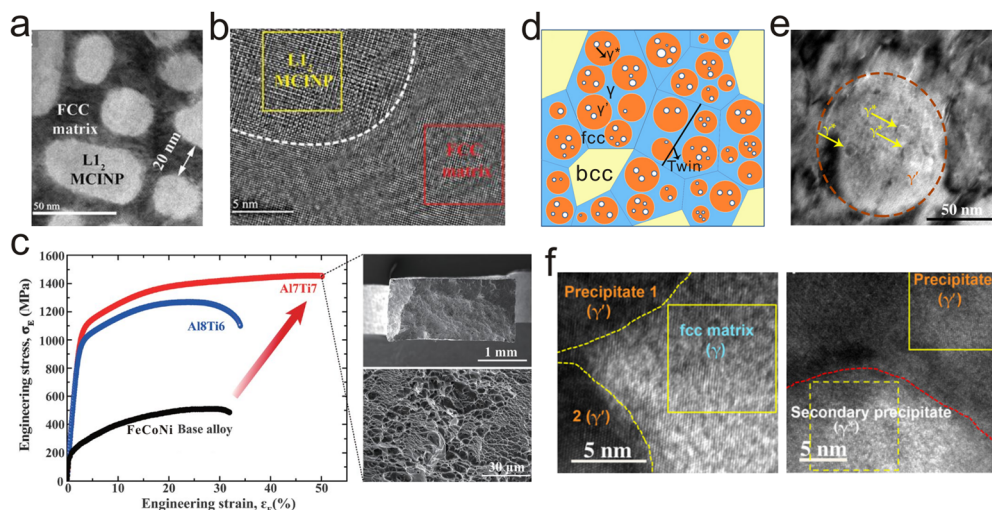


**Fig. 10** Construction of precipitation–matrix interfaces in HEAs. (a) TEM image of the alloy with the dual-phase region. (b) Magnified TEM image of the precipitation–matrix interface. (c) Engineering stress–strain curves (left) of the designed (FeCoNi)<sub>86</sub>–Al<sub>7</sub>Ti<sub>7</sub>(Al<sub>7</sub>Ti<sub>7</sub>) and (FeCoNi)<sub>86</sub>–Al<sub>8</sub>Ti<sub>6</sub>(Al<sub>8</sub>Ti<sub>6</sub>), as well as the FeCoNi-based alloy for comparison. The Al<sub>7</sub>Ti<sub>7</sub> alloy showed a ductile structure without macroscopic necking (right). Reproduced from ref. 149 with permission from American Association for the Advancement of Science, Copyright 2018. (d) Schematic illustration of the phase constitution in the alloy. (e) TEM image of the  $\gamma'$  nanoprecipitate is highlighted by the red circle and some secondary nanoprecipitates ( $\gamma^*$ ) are indicated by the arrows. (f) HRTEM image of the interface between the matrix ( $\gamma$ ) and two precipitates ( $\gamma'$ ) (left), and the interface between the precipitate ( $\gamma'$ ) and the secondary precipitate ( $\gamma^*$ ) (right), respectively. Reproduced from ref. 150 with permission from the American Association for the Advancement of Science, Copyright 2018.

deformation occurred, the constructed interface could contribute to decreasing the local stress–strain concentrations and inhibiting the nucleation of microcracks, thus achieving a promotion of mechanical properties (Fig. 10c). Furthermore, other researchers have reported different kinds of precipitation–matrix interfaces to enhance the mechanical properties. Chen *et al.* synthesized a bulk FeCoNiAlTi HEA that contained an FCC matrix and hierarchical nanoprecipitates by combining mechanical alloying with a spark plasma sintering strategy.<sup>150</sup> The high density of nanoprecipitates (denoted as  $\gamma'$ ) was present inside the FCC phase (denoted as  $\gamma$ ). Some secondary precipitates (represented by  $\gamma^*$ ) existed in the  $\gamma'$  precipitate (Fig. 10d and e). The hierarchical nanoprecipitates provided a more abundant interface of phases. Since there was a coherency of the  $\gamma$  matrix,  $\gamma'$  and  $\gamma^*$  phases (Fig. 10f), the dislocation-shearing mechanism was suspected to be the main precipitation strengthening factor. The HEA exhibited an ultimate tensile strength of about 2.52 GPa and an appreciable failure strain of about 5.2%.

Compared with designing the interface to enhance the mechanical properties in the bulk HEA, the development of HEA-NPs with a well-defined interface is still at the beginning, whose influence on the application deserves to be further explored and experimentally demonstrated. Chard *et al.* realized a series of thermodynamically stable polyelemental nanoparticles through a scanning probe block copolymer lithography strategy, providing an effective way to investigate the multiphase and interface formation at the nanoscale.<sup>56</sup> The reduction, nucleation, and growth of multiple elements occurred in the restricted space was defined using the polymer nanoreactor. Two-step long-term thermal annealing would

induce the aggregation of the metal ions within the polymer and further coarsening into a single nanoparticle, enabling the nanoparticles to reach thermodynamic equilibrium. They discovered that the nanoparticle composed of miscible elements exhibited the homogeneous elemental distribution. However, phase segregation was observed in the nanoparticle with immiscible elements. For instance, owing to the immiscibility of Au with Co and Ni, the quinary alloy nanoparticles (Au, Ag, Cu, Co, and Ni) exhibited three phases of AuAg/AuCu/CoNi. Afterward, they further discussed the number and types of interfaces formed by phase boundaries.<sup>55</sup> For the polyelemental nanoparticles, their thermodynamically preferential interface architecture was the one that possessed the lowest total surface and interfacial energies. For instance, based on the miscibility relationship among the Au, Co, Pd, and Sn, this quaternary system developed into Au, Co, and Pd<sub>3</sub>Sn phases. DFT calculations on the surface and interface energy of all possible interface structures revealed that the triphase Au/Co/Pd<sub>3</sub>Sn nanoparticles with three interface structures had the lowest total energy, which was consistent with the experimental result. Such discoveries offer us a good prediction for the thermodynamically stable phases and interface structures of polyelemental systems. Later, they achieved the synthesis of polyelemental heterostructured nanoparticles with high-index facets through alloying/dealloying with Bi.<sup>151</sup> The number and type of interface can be altered during the alloying process with Bi owing to the miscibility difference between Bi and different elements.

Recently, Hu *et al.* found that the complete random mixing of elements in the RhPtPdFeCo system transformed into a local single elemental ordering feature by replacing Rh with Ru.<sup>152</sup>



The increase of the Ru concentration would generate a distinct heterostructure with two interfaces of PtPdFeCo/Ru-rich/PtPdFeCo phases. The free energy change obtained by DFT calculations revealed that the introduction of Ru into PtPdFeCo increased the energy of the original system and then formed phase segregation to decrease the energy. Furthermore, Huang *et al.* demonstrated the nanometer-precision manipulation on phase segregation of polyelemental nanomaterials.<sup>153</sup> The layer growth mechanism at the interface of heterostructures induced by the small lattice mismatch facilitated the unit-cell-level interface engineering, leading to the synthesis of several phase-segregated segments with a unit-cell thickness in one single particle.

It is worth mentioning that the bulk phase diagrams may not be applicable to guiding the phase separation behavior of nanoparticles. For instance, it has been experimentally observed that the immiscible elements achieved uniform mixing within the nanoparticles.<sup>47</sup> The miscibility change is largely attributed to the surface effect of the small nanoparticles. In particular, the surface atoms possess fewer neighboring atoms than those in bulk, decreasing the interaction between immiscible elements and thus promoting the mixing. Additionally, the strain induced by the lattice mismatch of distinct elements can be relieved by the structural relaxation and defects of nanoparticles, further complicating the thermodynamic state of systems and influencing the separation at the nanoscale. Yang *et al.* revealed that the phase separation behavior of nanoparticles was largely affected by their composition, size, and possible surface absorbates.<sup>154</sup> Therefore, combined with the intrinsic element miscibility difference, these factors should be taken into consideration in the case of designing the phase interface of HEA-NPs.

## 5. Conclusions and perspectives

Interest in HEAs is increasing dramatically in the scientific community due to their remarkable properties as structural and functional materials. To further promote their exploration and practical applications, the synthesis of HEAs with controllable manufactured structures is urgently required. This review starts with a brief introduction of the fundamental parameters and advanced characterization methods related to HEAs. Subsequently, the recent progress in the controllable synthesis of HEAs is summarized from these aspects, namely, the composition, morphology, structure, and surface/interface. The chemical composition of HEAs can be designed by high-entropy mixing and element modulation. The morphology control involves the synthesis of different dimensional HEAs. The structure of HEAs can be constructed to form the solid solution, intermetallic, amorphous phase, and quasicrystal. The surface/interface can be engineered by modification, reconstruction, and multi-phase construction. The specific synthesis strategies and significance are also presented in the corresponding section, which would provide a clear guideline for realizing the controllable synthesis of HEAs. Generally, the

reported synthesis strategies demonstrated the controllability up to the nanoscale on the regulation of HEAs. Nanosized HEA products (*e.g.*, nanoparticles, nanowires, and nanosheets) and HEAs with nanostructures (*e.g.*, nanoporous structure, hollow nanostructure, and nanosized phase interface) could be obtained. When the element modulation is investigated, the atomic arrangement and distribution state could be regulated, exhibiting the possibility of atomic-precision manipulation.

In spite of the exciting advances made in the controllable synthesis of HEAs, several challenges still need to be explored. First, due to the compositional and structural complexity of HEAs, the current controllable fabrication of HEAs with different aspects is quite limited. The synthesis of HEAs with tailored composition, size uniformity, distinct morphology, exposed facets, hybrid structures (*e.g.*, core-shell, hierarchical and heterostructures), and unconventional phases should be given more attention, which would provide abundant active sites and reaction selectivity, enhance the stability and attain multi-functionalization. Two-dimensional HEAs with several atomic layer thicknesses could have innovative physical properties for next-generation quantum and optoelectronic devices. The exploration of short-range order, complex phase interface, and the accurate control of the ratio and distribution of every phase will conduce to the discovery of high-performance structural HEAs. All of these require the balance between current nonequilibrium techniques with the delicate control of HEAs, which can gain inspiration from existing wet chemistry. Besides, the development of mild and facile approaches would provide an opportunity for the precise regulation of HEAs in a high-yield way. Second, an in-depth understanding of growth mechanisms and dynamic evolution under operation conditions is crucial to guide the refined synthesis of HEAs and accelerate the development of applications. *In situ* characterization techniques enable us to detect multiscale information on HEAs in real time. *In situ* liquid or environmental electron microscopies can visualize the growth behavior of HEAs and even the change of the composition and structure during the growth process, which will provide valuable insight into the comprehensive understanding of the growth mechanism. The relationship between the phase structure and the mechanical property can be revealed by utilizing *in situ* TEM to observe the structural deformation of HEAs under strain. Moreover, *in situ* technology (*e.g.*, X-ray absorption spectroscopy, hard X-ray photoemission spectroscopy, and Raman spectroscopy) can offer information about chemical valence states, electronic structures, and even active sites, deepening the exploration of catalytic mechanisms. Based on the fundamental understanding of structure-to-property in the complicated system, HEAs can be controllably engineered more effectively as desired. Third, owing to essentially infinite combinations of elements, thus far, “tailoring” of HEAs seems to be mostly done experimentally in a random fashion. The elaborate “tailoring” requires the identification of functional units in certain applications and figuring out the role of individual elements and their correlation with the cocktail effect. High-throughput computational approach, especially the newly developed

machine learning techniques, provides great convenience to screen out and reasonably design HEAs with desired properties. Combined with high-throughput experiments, the correlation between the composition to structure and properties will be established to benefit the controllable synthesis of HEAs. Fourth, the future development of HEAs needs to expand the application fields as well. Structure engineering of HEAs mainly concentrates on the mechanical properties at present, whose effect on catalysis is worthy of investigation. Besides mechanical and catalytic applications, HEAs would be greatly possible to be applied in the fields of photocatalysis, biomedicine, and plasmonic fields given their unexpected features in vast composition space, all of which call for a reasonable design of HEAs on demand. Furthermore, the exploration of the integrating functional with mechanical properties is highly encouraged. In short, there is no doubt that the controllable synthesis of HEAs is extremely desirable and will be booming, thus promoting further research and diverse practical applications.

## Conflicts of interest

There are no conflicts to declare.

## Acknowledgements

This research was supported by the National Natural Science Foundation of China (Grant 22025303) and the National Key Research and Development Program of China (Grant 2022YFA1402501).

## Notes and references

- J. W. Yeh, S. K. Chen, S. J. Lin, J. Y. Gan, T. S. Chin, T. T. Shun, C. H. Tsau and S. Y. Chang, *Adv. Eng. Mater.*, 2004, **6**, 299–303.
- B. Cantor, I. T. H. Chang, P. Knight and A. J. B. Vincent, *Mater. Sci. Eng., A*, 2004, **375–377**, 213–218.
- D. B. Miracle and O. N. Senkov, *Acta Mater.*, 2017, **122**, 448–511.
- J. T. Ren, L. Chen, H. Y. Wang and Z. Y. Yuan, *Chem. Soc. Rev.*, 2023, **52**, 8319–8373.
- Y. Mei, Y. Feng, C. Zhang, Y. Zhang, Q. Qi and J. Hu, *ACS Catal.*, 2022, **12**, 10808–10817.
- O. El-Atwani, N. Li, M. Li, A. Devaraj, J. K. S. Baldwin, M. M. Schneider, D. Sobieraj, J. S. Wróbel, D. Nguyen-Manh, S. A. Maloy and E. Martinez, *Sci. Adv.*, 2019, **5**, eaav2002.
- Z. Li, K. G. Pradeep, Y. Deng, D. Raabe and C. C. Tasan, *Nature*, 2016, **534**, 227–230.
- S. Praveen and H. S. Kim, *Adv. Eng. Mater.*, 2018, **20**, 1700645.
- H. Li, J. Lai, Z. Li and L. Wang, *Adv. Funct. Mater.*, 2021, **31**, 2106715.
- S. Liu, Y. Wang, T. Jiang, S. Jin, M. Sajid, Z. Zhang, J. Xu, Y. Fan, X. Wang, J. Chen, Z. Liu, X. Zheng, K. Zhang, Q. Nian, Z. Zhu, Q. Peng, T. Ahmad, K. Li and W. Chen, *ACS Nano*, 2024, **18**, 4229–4240.
- Y. Liao, Y. Li, R. Zhao, J. Zhang, L. Zhao, L. Ji, Z. Zhang, X. Liu, G. Qin and X. Zhang, *Natl. Sci. Rev.*, 2022, **9**, nwac041.
- J. Ren, Y. Zhang, D. Zhao, Y. Chen, S. Guan, Y. Liu, L. Liu, S. Peng, F. Kong, J. D. Poplawsky, G. Gao, T. Voisin, K. An, Y. M. Wang, K. Y. Xie, T. Zhu and W. Chen, *Nature*, 2022, **608**, 62–68.
- Y. Ma, Y. Ma, Q. Wang, S. Schweidler, M. Botros, T. Fu, H. Hahn, T. Brezesinski and B. Breitung, *Energy Environ. Sci.*, 2021, **14**, 2883–2905.
- Y. Sun and S. Dai, *Sci. Adv.*, 2021, **7**, eabg1600.
- Z. Zhu, T. Jiang, M. Ali, Y. Meng, Y. Jin, Y. Cui and W. Chen, *Chem. Rev.*, 2022, **122**, 16610–16751.
- Y. Ai, M.-Q. He, H. Sun, X. Jia, L. Wu, X. Zhang, H.-B. Sun and Q. Liang, *Adv. Mater.*, 2023, **35**, 2302335.
- S.-G. Jung, Y. Han, J. H. Kim, R. Hidayati, J.-S. Rhyee, J. M. Lee, W. N. Kang, W. S. Choi, H.-R. Jeon, J. Suk and T. Park, *Nat. Commun.*, 2022, **13**, 3373.
- Y. Zhang, Y. N. Osetsky and W. J. Weber, *Chem. Rev.*, 2022, **122**, 789–829.
- E. Ma and X. Wu, *Nat. Commun.*, 2019, **10**, 5623.
- T. Löffler, A. Ludwig, J. Rossmeisl and W. Schuhmann, *Angew. Chem., Int. Ed.*, 2021, **60**, 26894–26903.
- T. Löffler, A. Savan, H. Meyer, M. Meischein, V. Strottkötter, A. Ludwig and W. Schuhmann, *Angew. Chem., Int. Ed.*, 2020, **59**, 5844–5850.
- X. Chang, M. Zeng, K. Liu and L. Fu, *Adv. Mater.*, 2020, **32**, 1907226.
- F. Xing, J. Ma, K. I. Shimizu and S. Furukawa, *Nat. Commun.*, 2022, **13**, 5065.
- Z. Li, Z. Zhang, X. Liu, H. Li, E. Zhang, G. Bai, H. Xu, X. Liu and X. Zhang, *Acta Mater.*, 2023, **254**, 118970.
- T. Ahmad, S. Liu, M. Sajid, K. Li, M. Ali, L. Liu and W. Chen, *Nano Res. Energy*, 2022, **1**, e9120021.
- E. P. George, D. Raabe and R. O. Ritchie, *Nat. Rev. Mater.*, 2019, **4**, 515–534.
- W. T. Koo, J. E. Millstone, P. S. Weiss and I. D. Kim, *ACS Nano*, 2020, **14**, 6407–6413.
- X. Wang, Q. Dong, H. Qiao, Z. Huang, M. T. Saray, G. Zhong, Z. Lin, M. Cui, A. Brozena, M. Hong, Q. Xia, J. Gao, G. Chen, R. Shahbazian-Yassar, D. Wang and L. Hu, *Adv. Mater.*, 2020, **32**, 2002853.
- Y. Li, Y. Liao, L. Ji, C. Hu, Z. Zhang, Z. Zhang, R. Zhao, H. Rong, G. Qin and X. Zhang, *Small*, 2022, **18**, 2107265.
- M. C. Gao, J.-W. Yeh, P. K. Liaw and Y. Zhang, *High-Entropy Alloys Fundamentals and Applications*, Springer, Switzerland, 2016.
- X. Wang, W. Guo and Y. Fu, *J. Mater. Chem. A*, 2021, **9**, 663–701.
- F. Otto, Y. Yang, H. Bei and E. P. George, *Acta Mater.*, 2013, **61**, 2628–2638.
- B. S. Murty, J. W. Yeh, S. Ranganathan and P. P. Bhattacharjee, *High-Entropy Alloys*, Elsevier, Netherlands, 2019.

- 34 A. Inoue, *Acta Mater.*, 2000, **48**, 279–306.
- 35 J. Feng, D. Chen, P. V. Pikhitsa, Y.-H. Jung, J. Yang and M. Choi, *Matter*, 2020, **3**, 1646–1663.
- 36 J. Y. He, W. H. Liu, H. Wang, Y. Wu, X. J. Liu, T. G. Nieh and Z. P. Lu, *Acta Mater.*, 2014, **62**, 105–113.
- 37 S. Guo, C. Ng, J. Lu and C. T. Liu, *J. Appl. Phys.*, 2011, **109**, 103505.
- 38 R. Chen, G. Qin, H. Zheng, L. Wang, Y. Su, Y. Chiu, H. Ding, J. Guo and H. Fu, *Acta Mater.*, 2018, **144**, 129–137.
- 39 Y. Dong, Y. Lu, L. Jiang, T. Wang and T. Li, *Intermetallics*, 2014, **52**, 105–109.
- 40 Q. Ding, Y. Zhang, X. Chen, X. Fu, D. Chen, S. Chen, L. Gu, F. Wei, H. Bei, Y. Gao, M. Wen, J. Li, Z. Zhang, T. Zhu, R. O. Ritchie and Q. Yu, *Nature*, 2019, **574**, 223–227.
- 41 R. Guo, L. Yu, Z. Liu, J. Pan, Y. Yao and L. Liu, *Nano Res.*, 2022, **15**, 4893–4901.
- 42 D. Wu, K. Kusada, T. Yamamoto, T. Toriyama, S. Matsumura, I. Gueye, O. Seo, J. Kim, S. Hiroi, O. Sakata, S. Kawaguchi, Y. Kubota and H. Kitagawa, *Chem. Sci.*, 2020, **11**, 12731–12736.
- 43 Y. Ding, H. Shi, M. Zeng and L. Fu, *Adv. Funct. Mater.*, 2022, **32**, 2202469.
- 44 D. Wu, K. Kusada, Y. Nanba, M. Koyama, T. Yamamoto, T. Toriyama, S. Matsumura, O. Seo, I. Gueye, J. Kim, L. S. Rosantha Kumara, O. Sakata, S. Kawaguchi, Y. Kubota and H. Kitagawa, *J. Am. Chem. Soc.*, 2022, **144**, 3365–3369.
- 45 D. Morris, Y. Yao, Y. Z. Finfrock, Z. Huang, R. Shahbazian-Yassar, L. Hu and P. Zhang, *Cell Rep. Phys. Sci.*, 2021, **2**, 100641.
- 46 Y. Ding, Z. Wang, Z. Liang, X. Sun, Z. Sun, Y. Zhao, J. Liu, C. Wang, Z. Zeng, L. Fu, M. Zeng and L. Tang, *Adv. Mater.*, 2023, DOI: [10.1002/adma.202302860](https://doi.org/10.1002/adma.202302860).
- 47 Y. Yao, Z. Huang, L. A. Hughes, J. Gao, T. Li, D. Morris, S. E. Zeltmann, B. H. Savitzky, C. Ophus, Y. Z. Finfrock, Q. Dong, M. Jiao, Y. Mao, M. Chi, P. Zhang, J. Li, A. M. Minor, R. Shahbazian-Yassar and L. Hu, *Matter*, 2021, **4**, 2340–2353.
- 48 J. Wang, P. Jiang, F. Yuan and X. Wu, *Nat. Commun.*, 2022, **13**, 1021.
- 49 Z. Su, T. Shi, H. Shen, L. Jiang, L. Wu, M. Song, Z. Li, S. Wang and C. Lu, *Scripta Mater.*, 2022, **212**, 114547.
- 50 X. Chen, Q. Wang, Z. Cheng, M. Zhu, H. Zhou, P. Jiang, L. Zhou, Q. Xue, F. Yuan, J. Zhu, X. Wu and E. Ma, *Nature*, 2021, **592**, 712–716.
- 51 Y. Yang, J. Zhou, F. Zhu, Y. Yuan, D. J. Chang, D. S. Kim, M. Pham, A. Rana, X. Tian, Y. Yao, S. J. Osher, A. K. Schmid, L. Hu, P. Ercius and J. Miao, *Nature*, 2021, **592**, 60–64.
- 52 Z. W. Chen, J. Li, P. Ou, J. E. Huang, Z. Wen, L. Chen, X. Yao, G. Cai, C. C. Yang, C. V. Singh and Q. Jiang, *Nat. Commun.*, 2024, **15**, 359.
- 53 Y. Zeng, B. Ouyang, J. Liu, Y.-W. Byeon, Z. Cai, L. J. Miara, Y. Wang and G. Ceder, *Science*, 2022, **378**, 1320–1324.
- 54 H. Wang, Q. He, X. Gao, Y. Shang, W. Zhu, W. Zhao, Z. Chen, H. Gong and Y. Yang, *Adv. Mater.*, 2024, **36**, 2305453.
- 55 P.-C. Chen, M. Liu, J. S. Du, B. Meckes, S. Wang, H. Lin, V. P. Dravid, C. Wolverton and C. A. Mirkin, *Science*, 2019, **363**, 959–964.
- 56 P.-C. Chen, X. Liu, J. L. Hedrick, Z. Xie, S. Wang, Q.-Y. Lin, M. C. Hersam, V. P. Dravid and C. A. Mirkin, *Science*, 2016, **352**, 1565–1569.
- 57 Y. Yao, Z. Huang, P. Xie, S. D. Lacey, R. J. Jacob, H. Xie, F. Chen, A. Nie, T. Pu, M. Rehwoldt, D. Yu, M. R. Zachariah, C. Wang, R. Shahbazian-Yassar, J. Li and L. Hu, *Science*, 2018, **359**, 1489–1494.
- 58 S. Gao, S. Hao, Z. Huang, Y. Yuan, S. Han, L. Lei, X. Zhang, R. Shahbazian-Yassar and J. Lu, *Nat. Commun.*, 2020, **11**, 2016.
- 59 M. Liu, Z. Zhang, F. Okejiri, S. Yang, S. Zhou and S. Dai, *Adv. Mater. Interfaces*, 2019, **6**, 1900015.
- 60 H. Jiang, X. Liu, M.-N. Zhu, J. Xu, L. An, P.-F. Sui, J.-L. Luo and G. J. Cheng, *Sci. Adv.*, 2022, **8**, eabm6541.
- 61 B. Wang, C. Wang, X. Yu, Y. Cao, L. Gao, C. Wu, Y. Yao, Z. Lin and Z. Zou, *Nat. Synth.*, 2022, **1**, 138–146.
- 62 M. W. Glasscott, A. D. Pendergast, S. Goines, A. R. Bishop, A. T. Hoang, C. Renault and J. E. Dick, *Nat. Commun.*, 2019, **10**, 2650.
- 63 K. Mori, N. Hashimoto, N. Kamiuchi, H. Yoshida, H. Kobayashi and H. Yamashita, *Nat. Commun.*, 2021, **12**, 3884.
- 64 H. Qiao, M. T. Saray, X. Wang, S. Xu, G. Chen, Z. Huang, C. Chen, G. Zhong, Q. Dong, M. Hong, H. Xie, R. Shahbazian-Yassar and L. Hu, *ACS Nano*, 2021, **15**, 14928–14937.
- 65 H. Minamihara, K. Kusada, T. Yamamoto, T. Toriyama, Y. Murakami, S. Matsumura, L. S. R. Kumara, O. Sakata, S. Kawaguchi, Y. Kubota, O. Seo, S. Yasuno and H. Kitagawa, *J. Am. Chem. Soc.*, 2023, **145**, 17136–17142.
- 66 K. Li and W. Chen, *Mater. Today Energy*, 2021, **20**, 100638.
- 67 T. Li, Y. Yao, Z. Huang, P. Xie, Z. Liu, M. Yang, J. Gao, K. Zeng, A. H. Brozena, G. Pastel, M. Jiao, Q. Dong, J. Dai, S. Li, H. Zong, M. Chi, J. Luo, Y. Mo, G. Wang, C. Wang, R. Shahbazian-Yassar and L. Hu, *Nat. Catal.*, 2021, **4**, 62–70.
- 68 M. D. Hossain, T. Borman, C. Osés, M. Esters, C. Toher, L. Feng, A. Kumar, W. G. Fahrenholtz, S. Curtarolo, D. Brenner, J. M. LeBeau and J. P. Maria, *Adv. Mater.*, 2021, **33**, 2102904.
- 69 M. Cui, C. Yang, B. Li, Q. Dong, M. Wu, S. Hwang, H. Xie, X. Wang, G. Wang and L. Hu, *Adv. Energy Mater.*, 2021, **11**, 2002887.
- 70 G. Cao, J. Liang, Z. Guo, K. Yang, G. Wang, H. Wang, X. Wan, Z. Li, Y. Bai, Y. Zhang, J. Liu, Y. Feng, Z. Zheng, C. Lu, G. He, Z. Xiong, Z. Liu, S. Chen, Y. Guo, M. Zeng, J. Lin and L. Fu, *Nature*, 2023, **619**, 73–77.
- 71 Y. Wang, W. Luo, S. Gong, L. Luo, Y. Li, Y. Zhao and Z. Li, *Adv. Mater.*, 2023, **35**, 2302499.
- 72 N. L. N. Broge, M. Bondesgaard, F. Søndergaard-Pedersen, M. Roelsgaard and B. B. Iversen, *Angew. Chem., Int. Ed.*, 2020, **59**, 21920–21924.
- 73 P. Zhao, Q. Cao, W. Yi, X. Hao, J. Li, B. Zhang, L. Huang, Y. Huang, Y. Jiang, B. Xu, Z. Shan and J. Chen, *ACS Nano*, 2022, **16**, 14017–14028.

- 74 X. He, Y. Zhang, X. Gu, J. Wang, J. Qi, J. Hao, L. Wang, H. Huang, M. Wen, K. Zhang and W. Zheng, *Nat. Commun.*, 2023, **14**, 775.
- 75 P. Xie, Y. Yao, Z. Huang, Z. Liu, J. Zhang, T. Li, G. Wang, R. Shahbazian-Yassar, L. Hu and C. Wang, *Nat. Commun.*, 2019, **10**, 4011.
- 76 R. Li, L. Xie, W. Y. Wang, P. K. Liaw and Y. Zhang, *Front. Mater.*, 2020, **7**, 290.
- 77 W. Chen, A. Hilhorst, G. Bokas, S. Gorsse, P. J. Jacques and G. Hautier, *Nat. Commun.*, 2023, **14**, 2856.
- 78 Y. Yao, Z. Liu, P. Xie, Z. Huang, T. Li, D. Morris, Z. Finfrock, J. Zhou, M. Jiao, J. Gao, Y. Mao, J. Miao, P. Zhang, R. Shahbazian-Yassar, C. Wang, G. Wang and L. Hu, *Sci. Adv.*, 2020, **6**, eaaz0510.
- 79 O. N. Senkov, J. D. Miller, D. B. Miracle and C. Woodward, *Nat. Commun.*, 2015, **6**, 6529.
- 80 R. Feng, C. Zhang, M. C. Gao, Z. Pei, F. Zhang, Y. Chen, D. Ma, K. An, J. D. Poplawsky, L. Ouyang, Y. Ren, J. A. Hawk, M. Widom and P. K. Liaw, *Nat. Commun.*, 2021, **12**, 4329.
- 81 T. A. A. Batchelor, J. K. Pedersen, S. H. Winther, I. E. Castelli, K. W. Jacobsen and J. Rossmeisl, *Joule*, 2019, **3**, 834–845.
- 82 Z. Lu, Z. W. Chen and C. V. Singh, *Matter*, 2020, **3**, 1318–1333.
- 83 T. Löffler, H. Meyer, A. Savan, P. Wilde, A. Garzón Manjón, Y.-T. Chen, E. Ventosa, C. Scheu, A. Ludwig and W. Schuhmann, *Adv. Energy Mater.*, 2018, **8**, 1802269.
- 84 Y. Yao, Z. Huang, T. Li, H. Wang, Y. Liu, H. S. Stein, Y. Mao, J. Gao, M. Jiao, Q. Dong, J. Dai, P. Xie, H. Xie, S. D. Lacey, I. Takeuchi, J. M. Gregoire, R. Jiang, C. Wang, A. D. Taylor, R. Shahbazian-Yassar and L. Hu, *Proc. Natl. Acad. Sci. U. S. A.*, 2020, **117**, 6316–6322.
- 85 T. A. A. Batchelor, T. Löffler, B. Xiao, O. A. Krysiak, V. Strotkötter, J. K. Pedersen, C. M. Clausen, A. Savan, Y. Li, W. Schuhmann, J. Rossmeisl and A. Ludwig, *Angew. Chem., Int. Ed.*, 2021, **60**, 6932–6937.
- 86 Y. Shi, Z. Lyu, M. Zhao, R. Chen, Q. N. Nguyen and Y. Xia, *Chem. Rev.*, 2021, **121**, 649–735.
- 87 X. Xia, S. Xie, M. Liu, H. C. Peng, N. Lu, J. Wang, M. J. Kim and Y. Xia, *Proc. Natl. Acad. Sci. U. S. A.*, 2013, **110**, 6669–6673.
- 88 Y. Xia, X. Xia and H.-C. Peng, *J. Am. Chem. Soc.*, 2015, **137**, 7947–7966.
- 89 Y.-H. Liu, C.-J. Hsieh, L.-C. Hsu, K.-H. Lin, Y.-C. Hsiao, C.-C. Chi, J.-T. Lin, C.-W. Chang, S.-C. Lin, C.-Y. Wu, J.-Q. Gao, C.-W. Pao, Y.-M. Chang, M.-Y. Lu, S. Zhou and T.-H. Yang, *Sci. Adv.*, 2023, **9**, eadf9931.
- 90 Z. Chen, J. Wen, C. Wang and X. Kang, *Small*, 2022, **18**, 2204255.
- 91 M. Xie, W. Fang, Z. Qu, Y. Hu, Y. Zhang, J. Chao, J. Shi, L. Wang, L. Wang, Y. Tian, C. Fan and H. Liu, *Nat. Commun.*, 2023, **14**, 1745.
- 92 H. Minamihara, K. Kusada, D. Wu, T. Yamamoto, T. Toriyama, S. Matsumura, L. S. R. Kumara, K. Ohara, O. Sakata, S. Kawaguchi, Y. Kubota and H. Kitagawa, *J. Am. Chem. Soc.*, 2022, **144**, 11525–11529.
- 93 Y. Yao, Z. Huang, P. Xie, T. Li, S. D. Lacey, M. Jiao, H. Xie, K. K. Fu, R. J. Jacob, D. J. Kline, Y. Yang, M. R. Zachariah, C. Wang, R. Shahbazian-Yassar and L. Hu, *ACS Appl. Mater. Interfaces*, 2019, **11**, 29773–29779.
- 94 T. Tsukamoto, T. Kambe, A. Nakao, T. Imaoka and K. Yamamoto, *Nat. Commun.*, 2018, **9**, 3873.
- 95 S. K. Kaiser, Z. Chen, D. Faust Akl, S. Mitchell and J. Perez-Ramirez, *Chem. Rev.*, 2020, **120**, 11703–11809.
- 96 P. Rao, Y. Deng, W. Fan, J. Luo, P. Deng, J. Li, Y. Shen and X. Tian, *Nat. Commun.*, 2022, **13**, 5071.
- 97 X. Lei, Q. Tang, Y. Zheng, P. Kidkhunthod, X. Zhou, B. Ji and Y. Tang, *Nat. Sustain.*, 2023, **6**, 816–826.
- 98 D. Huo, M. J. Kim, Z. Lyu, Y. Shi, B. J. Wiley and Y. Xia, *Chem. Rev.*, 2019, **119**, 8972–9073.
- 99 L. Tao, M. Sun, Y. Zhou, M. Luo, F. Lv, M. Li, Q. Zhang, L. Gu, B. Huang and S. Guo, *J. Am. Chem. Soc.*, 2022, **144**, 10582–10590.
- 100 Y. Sun, W. Zhang, Q. Zhang, Y. Li, L. Gu and S. Guo, *Matter*, 2023, **6**, 193–205.
- 101 C. Zhan, Y. Xu, L. Bu, H. Zhu, Y. Feng, T. Yang, Y. Zhang, Z. Yang, B. Huang, Q. Shao and X. Huang, *Nat. Commun.*, 2021, **12**, 6261.
- 102 H. Li, M. Sun, Y. Pan, J. Xiong, H. Du, Y. Yu, S. Feng, Z. Li, J. Lai, B. Huang and L. Wang, *Appl. Catal., B*, 2022, **312**, 121431.
- 103 D. Fan, K. Guo, Y. Zhang, Q. Hao, M. Han and D. Xu, *J. Colloid Interface Sci.*, 2022, **625**, 1012–1021.
- 104 M. Zeng, Y. Xiao, J. Liu, K. Yang and L. Fu, *Chem. Rev.*, 2018, **118**, 6236–6296.
- 105 Y. Chen, Z. Fan, Z. Zhang, W. Niu, C. Li, N. Yang, B. Chen and H. Zhang, *Chem. Rev.*, 2018, **118**, 6409–6455.
- 106 X. Fu, J. Zhang, S. Zhan, F. Xia, C. Wang, D. Ma, Q. Yue, J. Wu and Y. Kang, *ACS Catal.*, 2022, **12**, 11955–11959.
- 107 W. Chen, S. Luo, M. Sun, X. Wu, Y. Zhou, Y. Liao, M. Tang, X. Fan, B. Huang and Z. Quan, *Adv. Mater.*, 2022, **34**, 2206276.
- 108 T. Wang, Q. He, J. Zhang, Z. Ding, F. Li and Y. Yang, *Mater. Today*, 2020, **36**, 30–39.
- 109 J. Kwon, S. Sun, S. Choi, K. Lee, S. Jo, K. Park, Y. K. Kim, H. B. Park, H. Y. Park, J. H. Jang, H. Han, U. Paik and T. Song, *Adv. Mater.*, 2023, **35**, 2300091.
- 110 H.-J. Qiu, G. Fang, J. Gao, Y. Wen, J. Lv, H. Li, G. Xie, X. Liu and S. Sun, *ACS Materials Lett.*, 2019, **1**, 526–533.
- 111 H. Li, H. Huang, Y. Chen, F. Lai, H. Fu, L. Zhang, N. Zhang, S. Bai and T. Liu, *Adv. Mater.*, 2023, **35**, 2209242.
- 112 H. Chen, M. Zhang, Y. Wang, K. Sun, L. Wang, Z. Xie, Y. Shen, X. Han, L. Yang and X. Zou, *Nano Res.*, 2022, **15**, 10194–10217.
- 113 Y. Yao, Q. Dong, A. Brozena, J. Luo, J. Miao, M. Chi, C. Wang, I. G. Kevrekidis, Z. J. Ren, J. Greeley, G. Wang, A. Anapolsky and L. Hu, *Science*, 2022, **376**, eabn3103.
- 114 Y. Yuan, Y. Wu, X. Tong, H. Zhang, H. Wang, X. J. Liu, L. Ma, H. L. Suo and Z. P. Lu, *Acta Mater.*, 2017, **125**, 481–489.
- 115 Y. Bu, Z. Li, J. Liu, H. Wang, D. Raabe and W. Yang, *Phys. Rev. Lett.*, 2019, **122**, 075502.



- 116 T. Yang, B. X. Cao, T. L. Zhang, Y. L. Zhao, W. H. Liu, H. J. Kong, J. H. Luan, J. J. Kai, W. Kuo and C. T. Liu, *Mater. Today*, 2022, **52**, 161–174.
- 117 M. Luo, Y. Sun, L. Wang and S. Guo, *Adv. Energy Mater.*, 2017, **7**, 1602073.
- 118 P. Shi, R. Li, Y. Li, Y. Wen, Y. Zhong, W. Ren, Z. Shen, T. Zheng, J. Peng, X. Liang, P. Hu, N. Min, Y. Zhang, Y. Ren, P. K. Liaw, D. Raabe and Y.-D. Wang, *Science*, 2021, **373**, 912–918.
- 119 Y.-J. Liang, L. Wang, Y. Wen, B. Cheng, Q. Wu, T. Cao, Q. Xiao, Y. Xue, G. Sha, Y. Wang, Y. Ren, X. Li, L. Wang, F. Wang and H. Cai, *Nat. Commun.*, 2018, **9**, 4063.
- 120 M. Cui, C. Yang, S. Hwang, M. Yang, S. Overa, Q. Dong, Y. Yao, A. H. Brozena, D. A. Cullen, M. Chi, T. F. Blum, D. Morris, Z. Finfrook, X. Wang, P. Zhang, V. G. Goncharov, X. Guo, J. Luo, Y. Mo, F. Jiao and L. Hu, *Sci. Adv.*, 2022, **8**, eabm4322.
- 121 G. Zhu, Y. Jiang, H. Yang, H. Wang, Y. Fang, L. Wang, M. Xie, P. Qiu and W. Luo, *Adv. Mater.*, 2022, **34**, 2110128.
- 122 C.-L. Yang, L.-N. Wang, P. Yin, J. Liu, M.-X. Chen, Q.-Q. Yan, Z.-S. Wang, S.-L. Xu, S.-Q. Chu, C. Cui, H. Ju, J. Zhu, Y. Lin, J. Shui and H.-W. Liang, *Science*, 2021, **374**, 459–464.
- 123 Y. Nakaya, E. Hayashida, H. Asakura, S. Takakusagi, S. Yasumura, K. I. Shimizu and S. Furukawa, *J. Am. Chem. Soc.*, 2022, **144**, 15944–15953.
- 124 H. Shi, X. Y. Sun, Y. Liu, S. P. Zeng, Q. H. Zhang, L. Gu, T. H. Wang, G. F. Han, Z. Wen, Q. R. Fang, X. Y. Lang and Q. Jiang, *Adv. Funct. Mater.*, 2023, **33**, 2214412.
- 125 J. Ma, F. Xing, Y. Nakaya, K.-I. Shimizu and S. Furukawa, *Angew. Chem., Int. Ed.*, 2022, **61**, e202200889.
- 126 J. F. Löffler, *Intermetallics*, 2003, **11**, 529–540.
- 127 Z. Jia, K. Nomoto, Q. Wang, C. Kong, L. Sun, L. C. Zhang, S. X. Liang, J. Lu and J. J. Kruzic, *Adv. Funct. Mater.*, 2021, **31**, 2101586.
- 128 S. Guo, Q. Hu, C. Ng and C. T. Liu, *Intermetallics*, 2013, **41**, 96–103.
- 129 M. Hao, Y. Wang, D. Chen, D. Wu, P. Li and H. Zhang, *J. Alloys Compd.*, 2022, **906**, 164303.
- 130 J. Johnny, Y. Li, M. Kamp, O. Prymak, S.-X. Liang, T. Krekeler, M. Ritter, L. Kienle, C. Rehbock, S. Barcikowski and S. Reichenberger, *Nano Res.*, 2022, **15**, 4807–4819.
- 131 H. Ma, L. Zhao, Z.-Y. Hu, D. Miao, R. Li, T. Sun, H. Tian, T. Zhang, H. Li, Y. Zhang and Z. He, *Sci. China Mater.*, 2021, **64**, 440–447.
- 132 T. Zhang, L. Zhao, H. Ma, S. Huang, L. You, Y. Zhang and Z. He, *J. Alloys Compd.*, 2022, **910**, 164867.
- 133 K. Zeng, J. Zhang, W. Gao, L. Wu, H. Liu, J. Gao, Z. Li, J. Zhou, T. Li, Z. Liang, B. Xu and Y. Yao, *Adv. Funct. Mater.*, 2022, **32**, 2204643.
- 134 W. Shi, H. Liu, Z. Li, C. Li, J. Zhou, Y. Yuan, F. Jiang, K. Fu and Y. Yao, *SusMat.*, 2022, **2**, 186–196.
- 135 P. Zhang, X. Hui, Y. Nie, R. Wang, C. Wang, Z. Zhang and L. Yin, *Small*, 2023, **19**, 2206742.
- 136 B. Lim, M. Jiang, P. H. C. Camargo, E. C. Cho, J. Tao, X. Lu, Y. Zhu and Y. Xia, *Science*, 2009, **324**, 1302–1305.
- 137 J. Li, H.-M. Yin, X.-B. Li, E. Okunishi, Y.-L. Shen, J. He, Z.-K. Tang, W.-X. Wang, E. Yücelen, C. Li, Y. Gong, L. Gu, S. Miao, L.-M. Liu, J. Luo and Y. Ding, *Nat. Energy*, 2017, **2**, 17111.
- 138 B. Song, Y. Yang, M. Rabbani, T. T. Yang, K. He, X. Hu, Y. Yuan, P. Ghildiyal, V. P. Dravid, M. R. Zachariah, W. A. Saidi, Y. Liu and R. Shahbazian-Yassar, *ACS Nano*, 2020, **14**, 15131–15143.
- 139 J. Chang, G. Wang, C. Li, Y. He, Y. Zhu, W. Zhang, M. Sajid, A. Kara, M. Gu and Y. Yang, *Joule*, 2023, **7**, 587–602.
- 140 Y. Zeng, M. Zhao, Z. Huang, W. Zhu, J. Zheng, Q. Jiang, Z. Wang and H. Liang, *Adv. Energy Mater.*, 2022, **12**, 2201713.
- 141 L. Gao, X. Cui, C. D. Sewell, J. Li and Z. Lin, *Chem. Soc. Rev.*, 2021, **50**, 8428–8469.
- 142 A. A. H. Tajuddin, M. Wakisaka, T. Ohto, Y. Yu, H. Fukushima, H. Tanimoto, X. Li, Y. Misu, S. Jeong, J.-I. Fujita, H. Tada, T. Fujita, M. Takeguchi, K. Takano, K. Matsuoka, Y. Sato and Y. Ito, *Adv. Mater.*, 2023, **35**, 2207466.
- 143 M. Lin, G.-H. Kim, J.-H. Kim, J.-W. Oh and J.-M. Nam, *J. Am. Chem. Soc.*, 2017, **139**, 10180–10183.
- 144 Y. Liu, J. Ding, F. Li, X. Su, Q. Zhang, G. Guan, F. Hu, J. Zhang, Q. Wang, Y. Jiang, B. Liu and H. B. Yang, *Adv. Mater.*, 2023, **35**, 2207114.
- 145 H. Wang, S. Xu, C. Tsai, Y. Li, C. Liu, J. Zhao, Y. Liu, H. Yuan, F. Abild-Pedersen, F. B. Prinz, J. K. Nørskov and Y. Cui, *Science*, 2016, **354**, 1031–1036.
- 146 Z.-C. Zhang, B. Xu and X. Wang, *Chem. Soc. Rev.*, 2014, **43**, 7870–7886.
- 147 J. Gu, F. Duan, S. Liu, W. Cha and J. Lu, *Chem. Rev.*, 2024, **124**, 1247–1287.
- 148 Y. Lu, Y. Dong, S. Guo, L. Jiang, H. Kang, T. Wang, B. Wen, Z. Wang, J. Jie, Z. Cao, H. Ruan and T. Li, *Sci. Rep.*, 2014, **4**, 6200.
- 149 T. Yang, Y. L. Zhao, Y. Tong, Z. B. Jiao, J. Wei, J. X. Cai, X. D. Han, D. Chen, A. Hu, J. J. Kai, K. Lu, Y. Liu and C. T. Liu, *Science*, 2018, **362**, 933–937.
- 150 Z. Fu, L. Jiang, J. L. Wardini, B. E. MacDonald, H. Wen, W. Xiong, D. Zhang, Y. Zhou, T. J. Rupert, W. Chen and E. J. Lavernia, *Sci. Adv.*, 2018, **4**, eaat8712.
- 151 L. Huang, H. Lin, C. Y. Zheng, E. J. Kluender, R. Golnabi, B. Shen and C. A. Mirkin, *J. Am. Chem. Soc.*, 2020, **142**, 4570–4575.
- 152 Z. Huang, T. Li, B. Li, Q. Dong, J. Smith, S. Li, L. Xu, G. Wang, M. Chi and L. Hu, *J. Am. Chem. Soc.*, 2024, **146**, 2167–2173.
- 153 J. Yu, Y. Yin and W. Huang, *Nat. Synth.*, 2023, **2**, 749–756.
- 154 P.-C. Chen, M. Gao, C. A. McCandler, C. Song, J. Jin, Y. Yang, A. L. Maulana, K. A. Persson and P. Yang, *Nat. Nanotechnol.*, 2024, DOI: [10.1038/s41565-024-01626-0](https://doi.org/10.1038/s41565-024-01626-0).